POLITECNICO DI MILANO

School of Industrial and Information Engineering

Programme of Physics Engineering

KTH

ROYAL INSTITUTE OF TECHNOLOGY

School of Engineering Sciences

Department of Applied Physics, Laser Physics Section

Study of Blue-Light-Induced Infrared Absorption in KTiOPO$_4$ and Its Isomorphs

Supervisor:

Roberta Ramponi

External Supervisor:

Carlota Canalias

Master Thesis edited by:

Valerio Maestroni

Id. number:

798874

Academic Year 2013-2014

Acknowledgments

This project has been developed at the Laser Physics department of KTH; thanks to the people who work there I had the chance to prove myself in a new constructive experience. I have to thank in particular Prof. Fredrik Laurell, Prof. Carlota Canalias and Prof. Valdas Pasiskevicius, they are the three professors of the group that made this possible. They trust young students and make them grow as engineers, teaching them how to stand on their own feet. I hope I've fulfilled their expectations on me.

I am grateful to my supervisor Prof. Roberta Ramponi, who helped me with the draft of this thesis and that recommended me to Prof. Fredrik Laurell for this experience abroad. She surely advised me wisely, since I had the chance to work exactly in the kind of place I was looking for.

Thanks to Staffan, as assistant supervisor he gave a fundamental contribution to the development of this project, and still I have to understand where he found the patience to answer all of my questions and to help me with everything I needed. He was not just a reliable supervisor, he was also a good friend, I wish him and his beautiful family all the best.

Whenever I needed some help everybody in the office was ready to leave his job and show me what to do (professors included). This is the kind of attitude that made me feel like part of the group, so, Nicky, Peter, Charlotte, Hoda, Andrius, Gustav, Patrik, Jungsong, Wenhua and Chang thanks to all of you, your support was very important.

Of course I'll never forget of my friends in Kista: Riaan, Sebastian, Edoardo, Antonis, I hope I'll see you again someday in my life, thanks for the great time with you.

A special thanks goes to my closest friends: Jacopo, Andrea, Sara, Antonio, Beatrice. I know it's not easy to stand a stubborn engineer for so many years, but the time with you has always been the best, so please, be patient.

Thanks to my love, Giulia, for supporting me every day since we met. You give me what I need to be a better person, these years with you have been wonderful.

This is the work that closes my career as a student. It has been almost 20 years long, and I arrived here thanks to the teachings of my mother and of my father. I hope in the future I'll be a parent as good as they have been with me and my sister.

Summary

Index of Figures

1.

2.

3.

4.

5.

Index of Tables

1.

2.

3.

5.

x

Abstract

Potassium Titanyl Phosphate (KTiOPO$_4$ or KTP) is one of the most used crystals in nonlinear optics. Because of its properties, such as the high transparency in the range from 0.35µm to 4.3µm, the large angular and thermal acceptances and the high nonlinear coefficient, it is broadly used for second harmonic generation (SHG) in intracavity or extracavity configurations and as an active medium for optical parametric oscillators (OPO) and generators (OPG). In the last decades many other isomorphs of KTP with improved optical or electrical features have been synthesized, such as KTA, RTA or RTP.

This work aims at studying an effect that arises in a large variety of nonlinear crystals: a reversible photochromic damage that limits SH conversion efficiency called Blue Light Induced Infrared Absorption (BLIIRA). Effects of BLIIRA have been reported before for CW exposure in different materials [43,44], and for exposure to pulses in KTP, Ce:KTP and RKTP [19,24,42]. Here we study this damaging process in different crystals from the KTP family, namely KTP, RKTP, KTA, RTP and RTA, showing how the exposure to picoseconds pulses at 400nm changes the absorption of IR light. We have recorded the dynamics and the effects of BLIIRA under different conditions in order to better understand the mechanisms behind it; in particular we have tested crystals at different temperatures and under the exposure to different pulse length and average power of the damaging beam.

The observation of the damaging for long exposures to blue pulses has shown similar features for KTP and RKTP in accordance with previous publications, while in some of the other materials it has been possible to observe effects that inhibit the growth of the absorption coefficient during illumination. The comparison between BLIIRA in KTP isomorphs has shown various features depending on conductivity and on the chemical composition. Measurements at higher temperatures are characterized by faster relaxation dynamics for the absorption coefficient. The study of the damage with different pulse length and average power of the absorption-inducing beam has showed new features of BLIIRA among the crystals of the KTP family.

Abstract

Il Titanilfosfato di Potassio (KTiOPO$_4$ o KTP) è uno dei cristalli più utilizzati nell'ambito dell'ottica non lineare. Date le sue proprietà, come l'alta trasparenza nel range da 0.35µm a 4.3µm, l'ampia accettanza angolare e termica e l'elevato coefficiente non lineare, è ampiamente usato per la generazione di seconda armonica sia integrato in cavità laser sia esternamente, nonché impiegato come mezzo attivo in OPO (oscillatori ottici parametrici) ed OPG (generatori ottici parametrici). Negli ultimi decenni sono stati sintetizzati molti altri isomorfi del KTP, con migliori proprietà ottiche ed elettriche, tra cui KTA, RTA e RTP.

L'obiettivo di questo lavoro è lo studio di un effetto che si presenta in diversi cristalli non lineari: un danneggiamento fotocromatico reversibile che limita l'efficienza di conversione nella generazione di seconda armonica chiamato Blue Light Induced Infrared Absorption (BLIIRA). Gli effetti di BLIIRA sono stati riportati in precedenti pubblicazioni per illuminazione in CW di diversi materiali [43,44], nonché per l'esposizione a luce impulsata in KTP, Ce:KTP e RKTP [19,24,42]. In questo elaborato viene studiato tale processo in diversi cristalli della famiglia del KTP, quali KTP, RKTP, KTA, RTP e RTA, mostrando come l'esposizione ad impulsi a picosecondi a 400nm modifichi il coefficiente di assorbimento per la luce nell'infrarosso. Abbiamo registrato le dinamiche e gli effetti di BLIIRA in differenti condizioni così da poter meglio comprenderne i meccanismi; in particolare abbiamo eseguito le misure per differenti temperature del cristallo e utilizzando diversi valori della durata degli impulsi e della potenza media del fascio responsabile del danneggiamento.

L'osservazione del danneggiamento per lunghi tempi d'esposizione agli impulsi blu ha mostrato simili caratteristiche per KTP e RKTP, in accordo con precedenti pubblicazioni, mentre in alcuni altri materiali è stato possibile osservare effetti che sembravano inibire la crescita del coefficiente di assorbimento durante l'illuminazione. Il confronto dell'effetto BLIIRA tra diversi isomorfi di KTP ha mostrato che esistono caratteristiche che dipendono della conduttività e dalla composizione chimica. Misure ad alte temperature sono caratterizzate da dinamiche di rilassamento del coefficiente di assorbimento più rapide. Lo studio del danneggiamento con diversa lunghezza degli impulsi e potenza media del fascio responsabile dell'assorbimento indotto ha mostrato nuove peculiarità del fenomeno BLIIRA tra gli isomorfi di KTP.

Introduction

In the last decades nonlinear optical materials technologies have known such a strong development that they have found applications in a large variety of fields, becoming more and more reliable and efficient. The most common uses are related with nonlinear frequency conversion and parametric generation of light, which both allow for building laser sources in a wide range of frequencies, going from the UV to the far IR.

Potassium Titanyl Phosphate ($KTiOPO_4$), commonly called KTP, is one of the most used nonlinear crystals because of its excellent properties, such as the high nonlinear coefficient and the high damage threshold, together with the wide transparency range and the broad angular and thermal acceptance.

The Laser Physics department of KTH, the Royal Institute of Technology of Stockholm, has developed in many years a strong expertise in the field of nonlinear optical materials, focusing mainly on the study of KTP and its isomorphs. The acquired knowledge about their properties and characteristics has allowed, amongst other things, for the development of new poling techniques for QPM applications and for the design of new laser sources at different wavelengths, establishing new records in conversion efficiency.

This thesis project has been proposed by the Laser Physics group with the aim of investigating the effects of BLIIRA, i.e. Blue Light Induced Infrared Absorption, a damaging mechanism that is present in many different nonlinear crystals and reduces efficiency of light conversion from the near IR to the blue range (around 400nm). The phenomenon is related to the formation of colour centres (grey-tracking), which generate when free electrons and holes are trapped by complexes of Ti^{4+} ions and Oxygen vacancies in the Ti-O-Ti chain or by Fe^{3+} ions [11].

We find descriptions of BLIIRA just in a few publications for KTP, Ce:KTP and Rb:KTP [19,24,42], while grey-tracking mechanisms (or infrared light-induced absorption, i.e. GRIIRA) occuring when green light instead of the blue one is generated in the crystal is much more documented because of the importance of KTP for Nd:YAG frequency doubling at 532nm [9,10,13,18]. Given the similarities between GRIIRA and BLIIRA we based our research on the results from both of them, in order to understand what kind of behaviour we should expect and what kind of measurements would introduce some useful novelty element.

The effects of BLIIRA have been studied on periodically poled crystals from the KTP family, namely PPKTP, PPRKTP, PPKTA, PPRTP and PPRTA, using a grey-tracking pulsed source at 400nm with pulse length of 30ps. We decided first to analyze the dynamics of the IR light absorption coefficient on several crystals from different vendors and with different conductivity; then we repeated some of the measurements varying the properties of the damaging beam (pulse length and average power) and the crystal temperature. The gathered data have shown interesting features indicating that the response can change considerably passing from one isomorph to another, where absorption coefficient doesn't just show larger or smaller values while shining blue light, but also completely different dynamics. The changes in the signal from measurements with different blue beam characteristics and temperature highlight some features regarding the formation and the decay of the colour centres involved in BLIIRA.

In Chapter 1 we shortly introduce the nonlinear optics theory that describes the use of periodically poled KTP for second harmonic generation via quasi-phase matching. An overview on properties, features and different applications for KTP and the KTP isomorphs that we are going to use is given in Chapter 2. In Chapter 3 we present grey-tracking and BLIIRA effect, with the studies on their mechanisms. Chapter 4 describes the setup built to measure the dynamics of the absorption coefficient for IR light, and the thermal lens technique on which it is based; an overview on the IR pump source features closes the section. In chapter 5 we present and analyze the data we have gathered.

2

1. Nonlinear Optics

Nonlinear optics studies the modifications of material properties due to interaction with light. Typically only laser radiation is intense enough to change these properties, and studies of nonlinear effects started right after the invention of the first laser by Maiman in the 60's, with the observation of second harmonic generation.

Nonlinear effects are so called because of the nonlinear dependence of the dipole moment per unit volume, i.e. the polarization, on the applied electromagnetic field. Second harmonic generation for instance depends quadratically on the field intensity, which means that the frequency-doubled beam intensity increases as the square of the intensity of the applied laser light. While for linear optics we have a polarization $P(t)$ that is related to the applied field $E(t)$ by the linear relationship:

$$P(t) = \chi^{(1)} E(t) \tag{1.1}$$

where $\chi^{(1)}$ is the linear susceptibility, in nonlinear optics we express $P(t)$ as a power series in the field strength $E(t)$ as:

$$\begin{aligned} P(t) &= \chi^{(1)} E(t) + \chi^{(2)} E^2(t) + \chi^{(3)} E^3(t) + \cdots \\ &= P^{(1)}(t) + P^{(2)}(t) + P^{(3)}(t) + \cdots \end{aligned} \tag{1.2}$$

where $\chi^{(2)}$ and $\chi^{(3)}$ are respectively the second- and the third-order nonlinear optical susceptibilities. In this vision we have considered an instantaneous response of the material to the electric field, which implies that it must be dispersionless and lossless. We will call $P^{(2)}$ and $P^{(3)}$ the second- and third-order nonlinear polarizations, and it is possible to consider their contribution separately in order to describe the related nonlinear effects. As it is usual for expansions in power series, going up to higher orders means considering smaller contributes, which means that higher order nonlinearities will be progressively of minor entity given their smaller coefficients. For our purposes we will focus on nonlinear effects of the second order, since they are the ones for which crystal of the KTP family are commonly used. Before starting with an analytical study of these phenomena we will now introduce them qualitatively.

1.1. Qualitative Description of Nonlinear Processes

1.1.1. Second Harmonic Generation

Second harmonic generation (SHG) occurs when an electromagnetic wave of frequency ω hits a noncentrosymmetric crystal, generating an internal polarization that oscillates at twice the frequency. Since the internal dipoles are oscillating at 2ω, remembering that Larmor's theorem states that accelerated charges generate an electromagnetic field, this will generate a beam coming out from the crystal at the same doubled frequency. The process can also be schematically represented as the generation of a photon at double frequency starting from two photons at frequency ω (figure 1.1).

$$E(t) = E e^{-i\omega t} + cc. \tag{1.3}$$

$$P^{(2)}(t) = \chi^{(2)} E^2(t) = 2\chi^{(2)} E E^* + (\chi^{(2)} E^2 e^{-i2\omega t} + cc.) \tag{1.4}$$
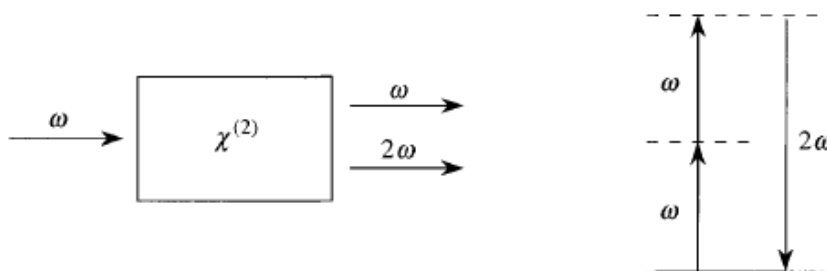
Figure 1.1 - Second harmonic generation scheme [25]

The rectified continuous wave component doesn't contribute for the generation of any electromagnetic wave, but results in a static electric field inside the crystal.

1.1.2. Sum- and Difference-Frequency Generation

Sum- and difference-frequency generation, being nonlinear effects of the second order, can be observed only in noncentrosymmetrical crystals where $\chi^{(2)}$ is different from zero. Here the incoming radiation consists of two frequency components, ω_1 and ω_2; the incident EM field and the induced polarization have the following form:

$$E(t) = E_1 e^{-i\omega_1 t} + E_2 e^{-i\omega_2 t} + cc. \tag{1.5}$$

4

$$P^{(2)}(t) = \chi^{(2)}\left[E_1^2 e^{-i2\omega_1 t} + E_2^2 e^{-i2\omega_2 t} + 2E_1 E_2 e^{-i(\omega_1+\omega_2)t}\right. \qquad (1.6)$$
$$\left. + 2E_1 E_2^* e^{-i(\omega_1-\omega_2)t}\right] + 2\chi^{(2)}\left[E_1 E_1^* + E_2 E_2^*\right]$$

We see that four electromagnetic waves are generated at frequencies $2\omega_1$, $2\omega_2$, $(\omega_1+\omega_2)$ and $(\omega_1-\omega_2)$; the first two cases consist of second harmonic generation, while the other two are respectively called sum frequency generation (SFG) and difference frequency generation (DFG). Also in this case we have an optical rectification forming a static field inside the crystal.

In sum frequency generation we have an analogy with the case of SHG, where we can summarize the process as the formation of a third photon starting from the combination of two photons from the incident radiation, i.e., considering the energy levels of the crystal's atom, we have a two-photon absorption process to a virtual level, and the subsequent decay (figure 1.2). The new frequency consists of the sum of the other two:

$$\omega_3 = \omega_1 + \omega_2 \qquad (1.7)$$
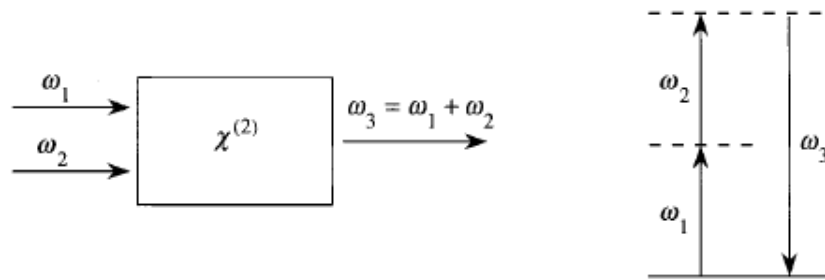
Figure 1.2 - Sum-frequency generation scheme [25]

Difference frequency generation follows a different mechanism, where a photon at higher frequency ω_1 is destroyed to form two photons at lower frequencies ω_2 and ω_3 (figure 1.3). What we obtain is not just the creation of radiation at frequency ω_3 but also an amplification of the signal at ω_2. This is the reason why this process is also called optical parametric amplification (OPA). Considering the energy levels of an atom of the crystal, we can imagine an absorption of the photon at energy $\hbar\omega_1$ and a spontaneous two photons decay with energy $\hbar\omega_2 + \hbar\omega_3$.
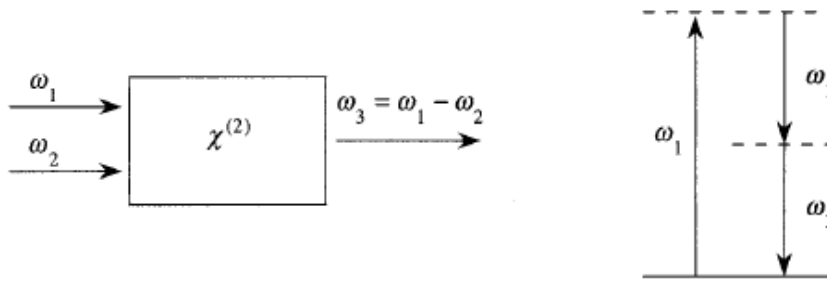
Figure 1.3 - Difference-frequency generation scheme [25]

The concept of optical parametric amplification can be extended inserting the nonlinear crystal inside an optical resonator and enhancing the amplification effect, obtaining an optical parametric oscillator (OPO), as the one sketched in figure 1.4. Both with OPA and OPO it is possible to generate light at any frequency lower than ω_1 just tuning the phase matching conditions (paragraph 1.3); usually these techniques are exploited to generate light at infrared wavelengths, where other laser sources are not available.
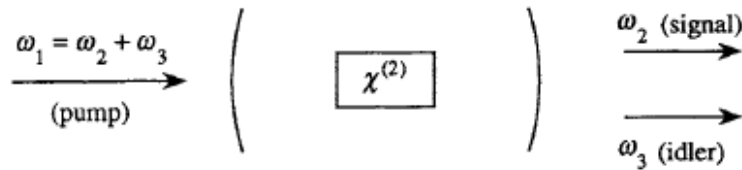
Figure 1.4 - OPO cavity for amplification of the signal ω_2 [25]

1.2. Quantitative Analysis of Nonlinear Processes

1.2.1. Wave Equation for Nonlinear Optical Media

We are considering two input field at frequencies ω_1 and ω_2, the material response is modelled as a combination of harmonic oscillators with frequency $\omega_1+\omega_2$. Each oscillator has a phase given by the phase of the incident field, but only under certain conditions of phase matching (paragraph 1.3) it is possible to obtain a constructive effect that actually produces a propagating wave travelling outside the crystal. The lack of phase matching results in a low conversion efficiency because of the destructive effects of dipoles oscillating with random phase.

We start from Maxwell's equations with some assumptions, considering the absence of free charges or free currents and a nonmagnetic material, so that:

6

$$\nabla \cdot \boldsymbol{D} = 0 \tag{1.8}$$

$$\nabla \cdot \boldsymbol{B} = 0 \tag{1.9}$$

$$\nabla \times \boldsymbol{E} = -\frac{1}{c}\frac{\partial \boldsymbol{B}}{\partial t} \tag{1.10}$$

$$\nabla \times \boldsymbol{H} = \frac{1}{c}\frac{\partial \boldsymbol{D}}{\partial t} \tag{1.11}$$

Given the material properties we have:

$$\boldsymbol{B} = \boldsymbol{H} \tag{1.12}$$

$$\boldsymbol{D} = \boldsymbol{E} + 4\pi\boldsymbol{P} \tag{1.13}$$

Taking the curl of equation (1.10), switching the order between the time derivative and the curl on $\boldsymbol{B}$, and considering equation (1.12) to substitute the curl of $\boldsymbol{B}$ with the right-hand side of equation (1.11) we obtain:

$$\nabla \times \nabla \times \boldsymbol{E} + \frac{1}{c^2}\frac{\partial^2 \boldsymbol{D}}{\partial t^2} = 0 \tag{1.14}$$

Using equation (1.13) we have:

$$\nabla \times \nabla \times \boldsymbol{E} + \frac{1}{c^2}\frac{\partial^2 \boldsymbol{E}}{\partial t^2} = -\frac{4\pi}{c^2}\frac{\partial^2 \boldsymbol{P}}{\partial t^2} \tag{1.15}$$

This form can be simplified remembering that:

$$\nabla \times \nabla \times \boldsymbol{E} = \nabla(\nabla \cdot \mathbf{E}) - \nabla^2 \mathbf{E} \tag{1.16}$$

The first term of the right-hand side vanishes for linear optics, while in our case, given the more complex relation between $\boldsymbol{D}$ and $\boldsymbol{E}$, it is null only if we assume that $\boldsymbol{E}$ is a transverse infinite plane wave. Even without this approximation it can be shown that in most of the cases the term is anyway small and negligible, so that the equation takes the form:

$$-\nabla^2 \mathbf{E} + \frac{1}{c^2}\frac{\partial^2 \boldsymbol{E}}{\partial t^2} = -\frac{4\pi}{c^2}\frac{\partial^2 \boldsymbol{P}}{\partial t^2} \tag{1.17}$$

It is convenient now to split the polarization term in a linear and a nonlinear part:

$$\boldsymbol{P} = \boldsymbol{P}^{(1)} + \boldsymbol{P}^{NL} \tag{1.18}$$

As a consequence also the displacement field is divided in linear and nonlinear:

$$\boldsymbol{D} = \boldsymbol{D}^{(1)} + 4\pi\boldsymbol{P}^{NL} \tag{1.19}$$

$$\boldsymbol{D}^{(1)} = \boldsymbol{E} + 4\pi\boldsymbol{P}^{(1)} \tag{1.20}$$

The wave equation can be expressed as:

$$-\nabla^2 \mathbf{E} + \frac{1}{c^2}\frac{\partial^2 \boldsymbol{D}^{(1)}}{\partial t^2} = -\frac{4\pi}{c^2}\frac{\partial^2 \boldsymbol{P}^{NL}}{\partial t^2} \qquad (1.21)$$

In a lossless and dispersionless medium the electric field and the displacement field are related by the dielectric tensor $\varepsilon^{(1)}$, that in the isotropic case is just a constant, $\varepsilon^{(1)}$, as:

$$\boldsymbol{D}^{(1)} = \varepsilon^{(1)}\boldsymbol{E} \qquad (1.22)$$

This finally brings us to the wave equation for nonlinear media:

$$-\nabla^2 \mathbf{E} + \frac{\varepsilon^{(1)}}{c^2}\frac{\partial^2 \boldsymbol{E}^{(1)}}{\partial t^2} = -\frac{4\pi}{c^2}\frac{\partial^2 \boldsymbol{P}^{NL}}{\partial t^2} \qquad (1.23)$$

This equation has the form of a driven wave equation, where the right-hand term is the source term. We will now consider each frequency component of the field separately, as:

$$\boldsymbol{E}(\boldsymbol{r},t) = \sum_n \boldsymbol{E}_n \qquad (1.24)$$

$$\boldsymbol{D}^{(1)}(\boldsymbol{r},t) = \sum_n \boldsymbol{D}_n^{(1)} \qquad (1.25)$$

$$\boldsymbol{P}^{NL}(\boldsymbol{r},t) = \sum_n \boldsymbol{P}_n^{NL} \qquad (1.26)$$

Where the components are represented in terms of their complex amplitude:

$$\boldsymbol{E}_n(\boldsymbol{r},t) = \boldsymbol{E}_n(\boldsymbol{r})e^{-i\omega_n t} + cc. \qquad (1.27)$$
$$\boldsymbol{D}_n^{(1)}(\boldsymbol{r},t) = \boldsymbol{D}_n^{(1)}(\boldsymbol{r})e^{-i\omega_n t} + cc. \qquad (1.28)$$
$$\boldsymbol{P}_n^{NL}(\boldsymbol{r},t) = \boldsymbol{P}_n^{NL}e^{-i\omega_n t} + cc. \qquad (1.29)$$

The wave equation (1.23) can be applied to each component, considering that the dielectric constant is frequency dependent, so that we have:

$$-\nabla^2 \mathbf{E}_n + \frac{\varepsilon^{(1)}}{c^2}\frac{\partial^2 \boldsymbol{E}_n^{(1)}}{\partial t^2} = -\frac{4\pi}{c^2}\frac{\partial^2 \boldsymbol{P}_n^{NL}}{\partial t^2} \qquad (1.30)$$

Taking the derivative of the fields over time we have:

$$-\nabla^2 \mathbf{E}_n(\boldsymbol{r}) - \frac{\omega_n^2}{c^2}\varepsilon^{(1)}(\omega_n)\boldsymbol{E}_n(\boldsymbol{r}) = \frac{4\pi\omega_n^2}{c^2}\boldsymbol{P}_n^{NL}(\boldsymbol{r}) \qquad (1.31)$$

1.2.2. Coupled Wave Equations

Starting from the equation (1.31) obtained in paragraph 1.2.1 we will consider now the generic situation of three wave mixing in order to deduce a system of coupled equations for the fields amplitudes that will be valid for sum- and difference-frequency generation as well as for second harmonic generation. We are considering a lossless nonlinear optical material and collimated, monochromatic, continuous wave input beams at normal incidence on the crystal surface.
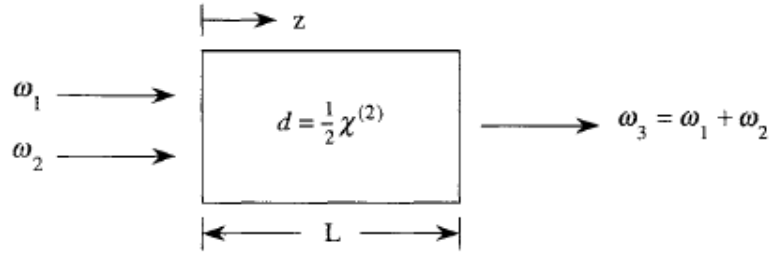
Figure 1.5 - Sum-frequency generation from a $\chi^{(2)}$ material [25]

Equation (1.31) holds for each frequency component, so if we consider now the case of sum-frequency generation depicted in figure 1.5, and the component at frequency ω_3, in absence of a source term it will have a solution of the form:

$$E_3(z,t) = A_3 e^{i(k_3 z - \omega_3 t)} + cc. \tag{1.32}$$

where A_3 is a constant. Including a source term, i.e. an interaction with the material, what we expect on physical ground is to obtain a solution with a similar form, but with an amplitude A_3 that becomes a slowly varying function of z. To solve the equation we consider the following form for the nonlinear polarization term and for the electric fields:

$$P_3(z,t) = P_3 e^{-i\omega_3 t} + cc. \tag{1.33}$$
$$E_i(z,t) = E_i e^{-i\omega_i t} + cc. \quad i = 1,2,3 \tag{1.34}$$

The amplitudes of the fields depend on z and have the form:

$$E_i = A_i e^{ik_i z} \tag{1.35}$$

From equation (1.6) we observe that considering the amplitude of the nonlinear polarization related to the sum-frequency factor and introducing the factor $d_{eff} = 1/2\chi^{(2)}$ we can write P_3 as:

$$P_3 = 4d_{eff} E_1 E_2 = 4d_{eff} A_1 A_2 e^{i(k_1 + k_2)z} = \tag{1.36}$$

$$= p_3 e^{i(k_1+k_2)z}$$

Substituting now equations (1.34), (1.35), (1.36) considering *i=3* inside the wave equation (1.31) obtained in the previous paragraph, and replacing ∇^2 with $\frac{\partial^2}{\partial z^2}$ since the field depends only on the longitudinal coordinate z, we obtain an equation for the amplitude of the sum-frequency wave:

$$\left[\frac{d^2A_3}{dz^2} + 2ik_3\frac{dA_3}{dz} - k_3^2A_3 + \frac{\varepsilon^{(1)}(\omega_3)\omega_3^2A_3}{c^2}\right]e^{i(k_3z-\omega_3t)} + cc.$$
$$= \frac{-16\pi d_{eff}\omega_3^2}{c^2}A_1A_2e^{i[(k_2+k_3)z-\omega_3t]} + cc. \tag{1.37}$$

The third and the fourth element on the left-hand side of the equation cancel, because $k_3^2 = \frac{\varepsilon^{(1)}(\omega_3)\omega_3^2}{c^2}$. We can drop the factor $e^{-i\omega_3t}$ on both sides and we can introduce the slowly-varying amplitude approximation, which states that:

$$\left|\frac{\partial^2A_3}{\partial z^2}\right| \ll \left|k_3\frac{\partial A_3}{\partial z}\right| \tag{1.38}$$

This way we can neglect the first term on the left-hand side and obtain:

$$\frac{dA_3}{dz} = \frac{8\pi d_{eff}\omega_3^2}{k_3c^2}A_1A_2e^{i\Delta kz} = \frac{2\pi i\omega_3}{n_3c}p_3e^{i\Delta kz} \tag{1.39}$$

In this form we have introduced the so called momentum mismatch *Δk*:

$$\Delta k = k_1+k_2 - k_3 \tag{1.40}$$

It is possible to proceed with analogous calculations for the amplitudes of the other two waves involved in the process, which bring us to a system of coupled amplitudes as follows:

$$\begin{cases} \dfrac{dA_1}{dz} = \dfrac{8\pi i d_{eff}\omega_1^2}{k_1c^2}A_3A_2^*e^{-i\Delta kz} \\[2mm] \dfrac{dA_2}{dz} = \dfrac{8\pi i d_{eff}\omega_2^2}{k_2c^2}A_3A_1^*e^{-i\Delta kz} \\[2mm] \dfrac{dA_3}{dz} = \dfrac{8\pi i d_{eff}\omega_3^2}{k_3c^2}A_1A_2e^{i\Delta kz} \end{cases} \tag{1.41}$$

It is easy to observe that the study of difference-frequency generation leads to the same equations, to calculate the output intensity the study will focus on the enhancement of the signal *A₂*, while for the case of sum-frequency

generation and second harmonic generation A_3 plays the role of the signal to generate.

In the end we can state that from this set of coupled equations it is possible to study any nonlinear effect of the second order and the evolution of each beam intensity. To give an example of the usage of this instrument, in the next paragraph we will perform the calculations for the case of second harmonic generation in a $\chi^{(2)}$ material.

1.2.3. Calculations for Second Harmonic Generation

For the case of second harmonic generation the beams involved in the process are just two, but we can imagine the fundamental beam as contributing with two photons for the generation of a single photon at double frequency. We will have then this relation between the amplitudes of the beams in the coupled equations and the amplitude of fundamental and second harmonic beam:

$$A_1 = A_2 = \frac{A_{SH}}{\sqrt{2}}$$
$$A_3 = A_{SH}$$

(1.42)

We then pass to a more compact notation using:

$$K_i = \frac{8\pi d_{eff}\omega_i^2}{k_i c^2}$$

(1.43)

The system is reduced to two coupled equations:

$$\begin{cases} \dfrac{dA_{FF}}{dz} = iK_{FF}A_{SH}A_{FF}^* e^{-i\Delta kz} \\ \dfrac{dA_{SH}}{dz} = iK_{SH}\dfrac{A_{FF}^2}{2} e^{i\Delta kz} \end{cases}$$

(1.44)

We introduce an approximation of low depletion of the fundamental beam, so that $A_{FF} = const.$ and we calculate the amplitude of the second harmonic wave integrating over the crystal length L.

$$A_{SH}(L) - A_{SH}(0) = i\frac{K_{SH}A_{FF}^2}{2}\int_0^L e^{i\Delta kz}dz$$

(1.45)

Starting from an initial condition where $A_{SH}(0)=0$ we can obtain the amplitude as a function of the crystal length and of the momentum mismatch:

$$A_{SH}(L) = i\frac{K_{SH}A_{FF}^2}{2}\frac{e^{i\Delta kL}-1}{i\Delta k} =$$

$$= i\frac{K_{SH}A_{FF}^2}{\Delta k}e^{i\frac{\Delta kL}{2}}\left(\frac{e^{i\frac{\Delta kL}{2}}-e^{-i\frac{\Delta kL}{2}}}{2i}\right) = \qquad (1.46)$$

$$= i\frac{K_{SH}A_{FF}^2}{\Delta k}e^{i\frac{\Delta kL}{2}}\sin\frac{\Delta kL}{2}$$

The intensity of the second harmonic beam is:

$$I_{SH}(L) = \frac{1}{2}c\varepsilon_0 n_{SH}|A_{FF}|^4\frac{K_{SH}^2}{\Delta k^2}sin^2\left(\frac{\Delta kL}{2}\right) \qquad (1.47)$$

The intensity of both fundamental and second harmonic beam is plotted against the quantity L/L_c in figure 1.6, where the coherence length L_c is defined as $L_c=\pi/\Delta k$
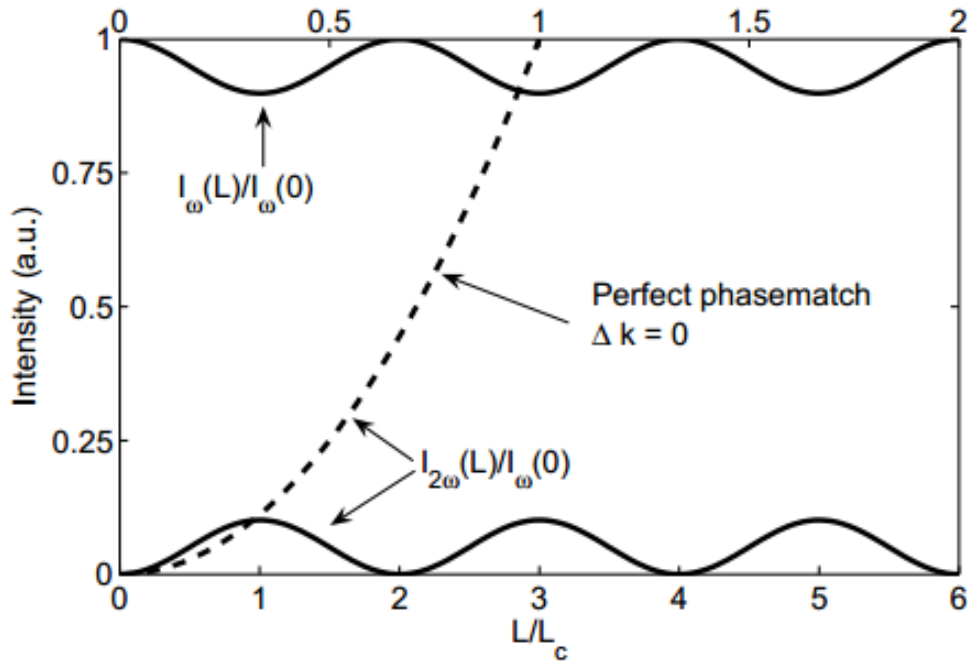
Figure 1.6 - Intensity of the fundamental and of the second-harmonic beam along the crystal length. The dashed line shows the quadratic increase of the second-harmonic radiation in case of phasematch

In the same figure is also represented the quadratic growth of the intensity for the particular case of phase matching, where $\Delta k=0$.

1.3. Phase Matching

The concept of phase matching has been introduced in paragraph 1.2.1 with the simple picture of harmonic oscillators excited by the incident beams and oscillating at the frequency ω_3. Without any additional hypothesis their phases are completely mismatched, which means that their contributes to the generation of the travelling wave at frequency ω_3 don't add constructively. The condition of phase matching between these oscillating dipoles is obtained when:

$$\Delta k = 0$$
$$k_3 = k_1 + k_2 \tag{1.48}$$

Let us now consider the coupled equation for the amplitude of the generated wave A_3 in (1.41); under the hypothesis of non-depleted pump, i.e. considering A_1 and A_2 constant, and considering an initial null amplitude $A_3(0)=0$, it is possible to integrate over the length L of the crystal to obtain:

$$
\begin{aligned}
A_3(L) &= \frac{8\pi i d_{eff} \omega_3^2 A_1 A_2}{k_3 c^2} \int_0^L e^{i\Delta k z} dz \\
&= \frac{8\pi i d_{eff} \omega_3^2 A_1 A_2}{k_3 c^2} \left(\frac{e^{i\Delta kL} - 1}{i\Delta k} \right)
\end{aligned}
\tag{1.49}
$$

The intensity of the generated wave is proportional to the modulus squared of the amplitude, so:

$$
\begin{aligned}
I_3 &\propto \left| \frac{e^{i\Delta kL} - 1}{i\Delta k} \right|^2 = L^2 \left(\frac{e^{i\Delta kL} - 1}{\Delta kL} \right) \left(\frac{e^{-i\Delta kL} - 1}{\Delta kL} \right) \\
&= 2L^2 \frac{(1 - \cos \Delta kL)}{(\Delta kL)^2} = \\
&= L^2 \frac{sin^2 \left(\frac{\Delta kL}{2} \right)}{\left(\frac{\Delta kL}{2} \right)^2} = L^2 sinc^2 \left(\frac{\Delta kL}{2} \right)
\end{aligned}
\tag{1.50}
$$

For perfect phase matching we obtain the highest intensity of the output beam, as shown in figure 1.7. Also considering the expression obtained for the intensity of the second harmonic radiation (equation (1.47)), we see that it increases as the square of the crystal length instead of oscillating as in the phase mismatched case (figure 1.6).
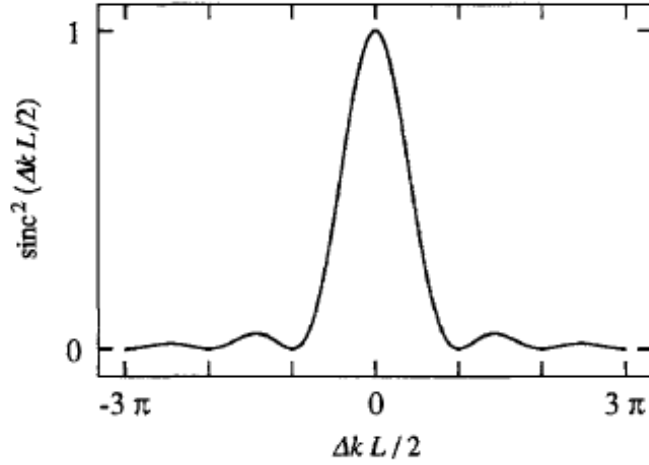
Figure 1.7 - Dependence of the generated radiation intensity on the momentum mismatch [25]

In the following sections, after showing how the phase mismatch arises due to the variation of refractive index with frequency, we will describe two different ways of achieving phase matching in nonlinear crystals.

1.3.1. Birefringent Phase Matching

To achieve the phase matching conditions we should have:

$$k_1 + k_2 = k_3 \tag{1.51}$$

Considering that $k_i = \frac{n_i \omega_i}{c}$ this can be written as:

$$n_1 \omega_1 + n_2 \omega_2 = n_3 \omega_3 \tag{1.52}$$

Which implies, for second harmonic generation where $\omega_1 = \omega_2$ and $\omega_3 = 2\omega_1$, having:

$$n(\omega_1) = n(2\omega_1) \tag{1.53}$$

While for the case of sum-frequency generation it can be shown after some simple calculation that the phase matching condition is obtained for:

$$n_3 - n_2 = (n_1 - n_2)\frac{\omega_1}{\omega_3} \tag{1.54}$$

Both conditions in (1.53) and (1.54) can't be fulfilled for the case of normal dispersion, as the refractive index is a monotone function in ω. This is the reason why one of the most used way of achieving high conversion efficiency is to use birefringent materials, where the refractive index depends on the direction of the polarization of the incident radiation.

14

Uniaxial birefringent crystals are characterized by an optic axis (or c axis). Light polarized perpendicular to the plane containing k and the optic axis experiences a refractive index n_o, while light polarized in the plane containing k and the optic axis experiences a refractive index $n_e(\theta)$ where θ is the angle between optic axis and k. $n_e(\theta)$ is calculated according to the equation:

$$\frac{1}{n_e^2(\theta)} = \frac{sin^2\theta}{n_e^2} + \frac{cos^2\theta}{n_o^2} \qquad (1.55)$$

In this formula n_e is the principal value of the extraordinary refractive index, obtained for $\theta = \pi$. We can distinguish between positive uniaxial crystals where $n_e > n_o$ and negative uniaxial crystals where $n_e < n_o$. The wave with the highest frequency is polarized in the direction that gives the lower of the two refractive indices in order to satisfy equation (1.53). It will have then an ordinary polarization if we use positive crystal, while for negative uniaxial crystals it will have extraordinary polarization. Depending on the orientation of the polarization for the lower-frequency waves we distinguish between Type I phase matching, where the orientation is the same for the two waves, and the Type II phase matching where they are orthogonal. Table 1.1 shows the possible cases for sum-frequency generation with positive and negative uniaxial crystals.

	Positive uniaxial ($n_e > n_o$)	Negative uniaxial ($n_o > n_e$)
Type I	$n_3^o\omega_3 = n_1^e\omega_1 + n_2^e\omega_2$	$n_3^e\omega_3 = n_1^o\omega_1 + n_2^o\omega_2$
Type II	$n_3^o\omega_3 = n_1^o\omega_1 + n_2^e\omega_2$	$n_3^e\omega_3 = n_1^e\omega_1 + n_2^e\omega_2$

Table 1.1

With proper orientation of the beams polarizations with respect of the optic axis of the crystal it is possible to obtain phase matching. For the simple case of second harmonic generation in a negative uniaxial crystal we have:

$$n_e(2\omega, \theta) = n_o(\omega) \qquad (1.56)$$

We can then calculate the angle of incidence between the propagation direction of the beam and the optic axis using:

$$\frac{sin^2\theta}{n_e^2(2\omega)} + \frac{cos^2\theta}{n_o^2(2\omega)} = \frac{1}{n_o^2(\omega)} \qquad (1.57)$$

Birefringence has a strong drawback, because it is well known that for values of θ different from 0 or π the waves with ordinary and extraordinary polarization will diverge when passing through the crystal, thus diminishing the amount of overlap and the overall conversion efficiency. For some crystals it is possible to tune birefringence with a temperature change, using an angle of 0 or π and obtaining phase matching without any loss caused by the lack of overlap.

1.3.2. Quasi-Phase Matching and Periodic Poling

In some cases it is not possible or feasible to obtain phase matching using birefringence. This happens when we want to exploit the d_{33} coefficient from the d_{eff} tensor for all of the beams, usually because it shows higher values than the off-diagonal ones, but this means having the same polarization for all of the interacting beam, without any exploitation of birefringence. In other cases the materials simply don't show any birefringence, or it is not strong enough to compensate for dispersion. As we have demonstrated in paragraph 1.2.3 for SHG, and as it is for many other situation of nonlinear generation, without phase matching we obtain an efficiency that oscillates over the crystal length L, as depicted in figure 1.8.
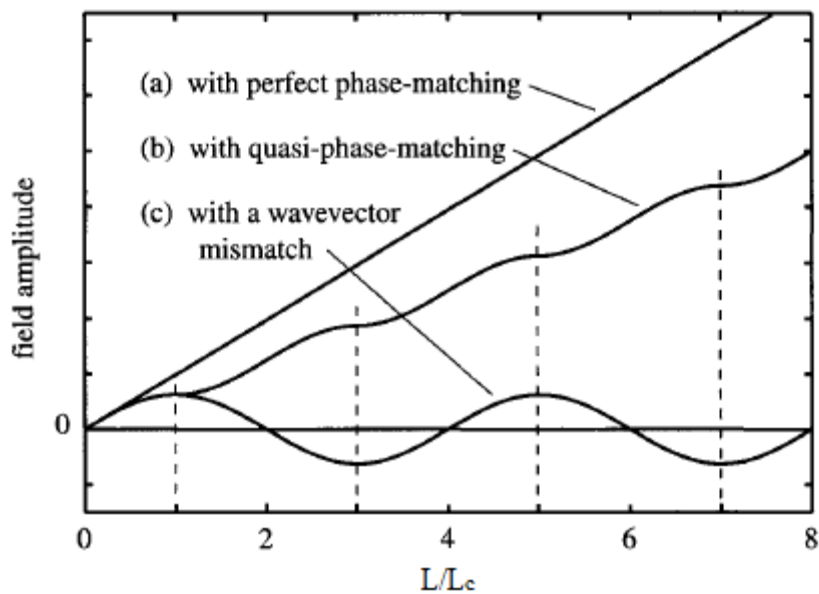
Figure 1.8 - Comparison between generated intensities in different phase-matching conditions [25]

An idea to obtain a constructive effect is to invert the position of the c axis periodically after a coherence length $\Lambda_{coh}=(2k+1)L_c$, so that the contribution for the next segment of length Λ_{coh} will add to the previous one, and so on.

16

Figure 1.8 shows that this way we obtain an electric field that doesn't grow linearly with L as in the phase matched case, but a considerable growth of the output beam and of the overall conversion efficiency.

Materials fabricated with the structure described above are called periodically poled materials. The periodic poling technique applies with excellent effects in ferroelectric materials, such as KTP, where a pattern of electrodes with alternated polarities is deposited on the sides of the crystal, and a strong electric field is used to rotate the ferroelectric domains, and as a consequence the c-axis, in an antiparallel configuration. It has been demonstrated that also polymeric materials can be periodically poled, and that it is also possible to directly grow crystals with a periodic alternation in the orientation of the c-axis.

2. KTiOPO$_4$ and Its Isomorphs

This chapter is aimed to introduce the reader to the main properties of Potassium Titanyl Phosphate, commonly referred to as KTiOPO$_4$ or KTP, and how they change among different isomorphs of the KTP family. After a description of the crystal structure, we analyze the ferromagnetic behaviour of the material and its conducting properties. Given the nature of our work we focus then on the linear and nonlinear optical properties, concluding with an overview on the studied isomorphs, showing how the differences in the crystalline structure lead to different features and suitable applications.

2.1. Crystal Structure

KTP crystals belong to the *mm2* class of the orthorhombic system, with noncentrosymmetric point space group *Pna2$_1$*. The atomic structure form a rather complicated three-dimensional framework that is usually simplified with the individuation of vertex-sharing TiO$_6$ octahedra, which compose together to form helical structures aligned along the c-axis and bond to each other by PO$_4$ tetrahedra, as shown in figure 2.1. The Potassium atoms are disposed along the helical channels in two crystallographic independent positions, identified as K(1) and K(2) and characterized by a different number of neighbouring oxygen atoms, respectively nine and eight for the two cases. The ionic conductivity shown by this material, that along the c-axis is two order of magnitude higher than in the two other directions, is due to the possibility for K+ cations to travel through the helical channels, and is enhanced by the presence of a higher concentration of Potassium vacancies. While the PO$_4$ tetrahedra between the helixes are undistorted, the Titanium atoms identified as Ti(1) and Ti(2) are slightly displaced from the centre of the octahedra, so that the chain of O-Ti(1)-O-Ti(2)-O atoms running along the helix shows an alternation of long and short bonds between the Oxygen and the Titanium atoms.

It has been hypothesized by Zumsteg [41] that the nonlinear optical behaviour of KTP derives from this distortion, giving to the nonlinear coefficient *d$_{33}$* such a high value, while in later studies [45] this effect has been related to the chemical bonds of the KO$_x$ and PO$_4$ groups.
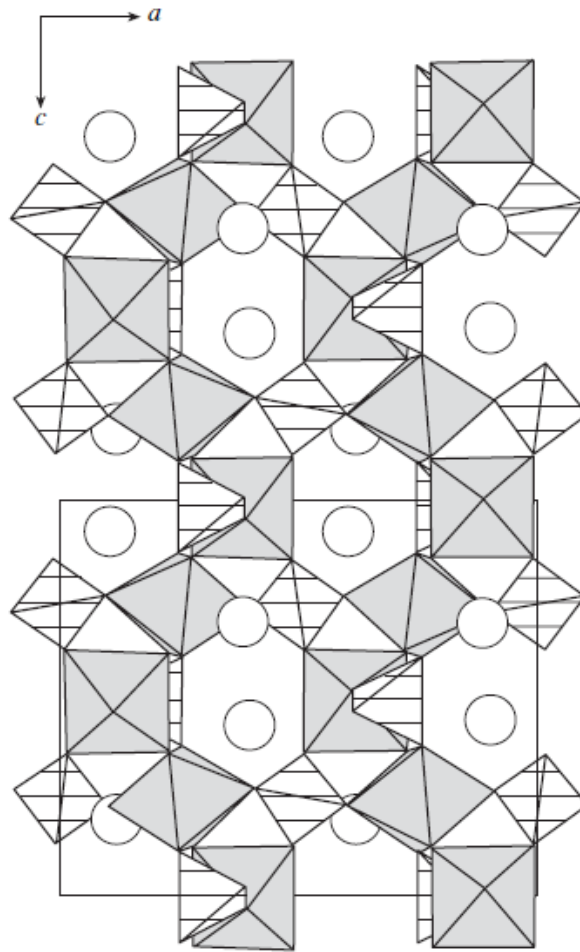
Figure 2.1 - KTiOPO$_4$ crystalline structure. The two helixes of vertex-sharing TiO$_6$ octahedra are connected by PO$_4$ tetrahedra and directed along the c-axis. The spheres represent the K$^+$ ions. [7]

2.2. Ferroelectric Properties and Periodic Poling

Potassium Titanyl Phosphate has a ferroelectric behaviour with 180° domains oriented along the c-axis and a Curie temperature that can vary from 928 to 965°C depending on the growth conditions and on the number of generated defects. The spontaneous polarization at room temperatures stands in the range between 16-24µC/cm^2. Studies of ferroelectric features have been performed observing the evolution of permittivity and of second harmonic intensity with increasing temperature [7].
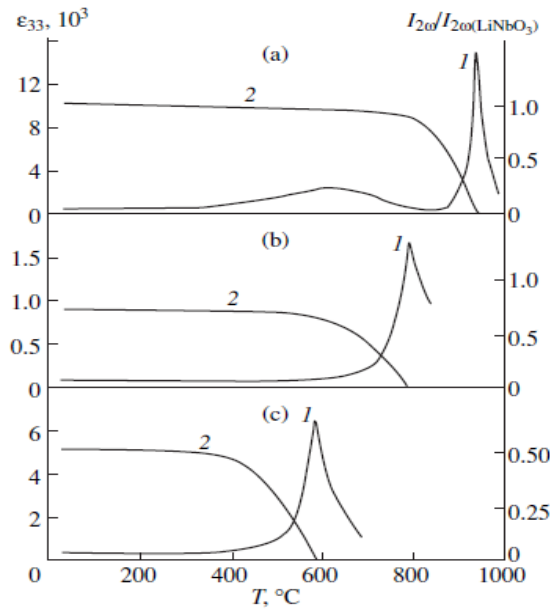
Figure 2.2 - Evolution of permittivity and SH signal intensity with increasing temperature in a) KTP, b) RTP and c) TTP [7]

In figure 2.2 it is possible to see how ε_{33} spikes when the Curie temperature is reached, as it is typical for ferroelectric phase transitions, while the intensity of the generated second harmonic decreases because of the change in symmetry and of the lost polarity in the new paramagnetic phase. The linear behaviour of the SH intensity in the vicinity of the transition point indicates a polarization with a temperature dependence of the form:

$$P_s = \sqrt{T - T_0} \tag{2.1}$$

which means that we are dealing with a second-order transition. The hysteresis loop is not observable at room temperature because it is masked by the high ionic current, but it has been recorded at 170K showing a spontaneous polarization of 23.7µC/cm², and a coercive field of 120kV/cm (figure 2.3) [52].
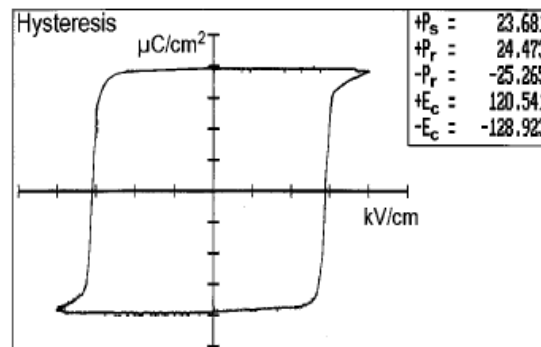
Figure 2.3 - Hysteresis loop of ferroelectric domains measured at 170K [52]

The study of ferroelectric domains [46], the refining of the techniques for single domain growth and domain engineering [3,28,47] have been crucial for the development of devices exploiting quasi-phase matching. Although several methods involving chemical reactions, e-beam writing and crystal growth control have been demonstrated over the years, the most diffuse technique to fabricate the periodic domain structure, and the one that has been used to pole the samples we used for our work, is the electric field poling. On one of the polar faces of the crystal it is deposited a thin layer of positive resist, which after a soft baking process is exposed through a mask to UV light. On the developed resist pattern the Al layer which will form the periodic structure of the electrodes is evaporated. The crystal is then mounted on an insulating holder, while the electrodes are immersed in an almost saturated solution of KCl, the electrolyte. In the end the material is connected to a circuit which poles it with electrical pulses reaching high peak values, in order to obtain antiparallel domains [1,28] (figure 2.4). Depending on the poling period, given by the mask pattern, the wavelength of the quasi-phase matched radiation will change. The high ionic conductivity (discussed in paragraph 2.3) represents a problem for KTP poling, since the current flow that is established inside the crystal can cause the breakdown of the material before the coercive field is reached. The Al layer deposited in between the liquid electrodes causes a strong decrease of the ionic conductivity, allowing for the periodic poling.

cutting & polishing
solvent cleaning

resist spinning (2 μm)
and baking (110°C, 90s)

resist exposure &
development

Al-deposition

Electric field poling
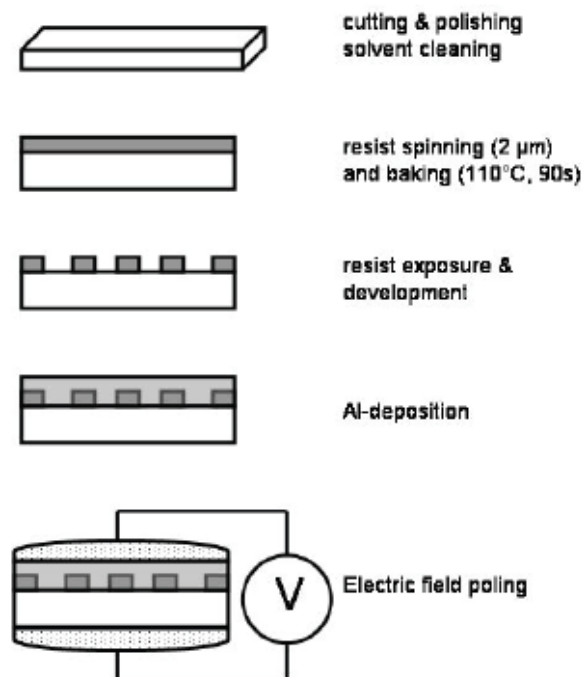
Figure 2.4 - Procedure for electric periodic poling [28]

22

2.3. Conducting Properties

The ionic conductivity, a property analyzed since the very first studies on KTP, is due to the hopping mechanism which allows for the Potassium atoms to move along the helical channels formed by the TiO_6 octahedra [2,4,7,8]. The process is activated by the presence of vacancies of K^+ atoms, whose number can be controlled changing the growth conditions. Considering the direction along the polar axis, conductivity can reach values up to 10^{-4}S/cm at room temperature, while the complete behaviour of $\sigma(T)$, excluding some anomalies occurring during the phase transition and caused by the domain walls motion, is well described by the Vogel-Fulcher-Tamman equation:

$$\sigma(T) = \sigma_0 e^{-\frac{E_a^{VFT}}{k(T-T_0)}}$$
(2.2)

where $E_a{}^{VFT}$ is the characteristic activation energy and T_0 is the temperature at which is possible to observe the freezing of the ionic contribution to conductivity; for the case of KTP it has been estimated $T_0 = 170K$ [7]. In figure 2.5 it is possible to observe the behaviour of conductivity at high temperatures.
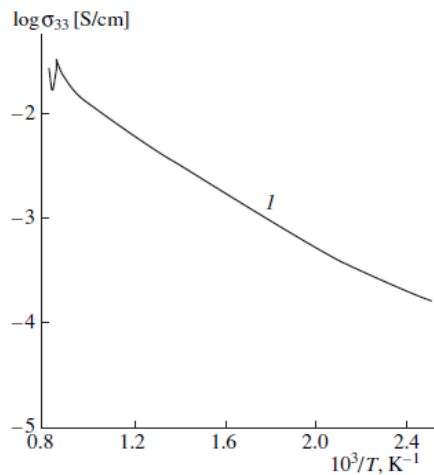
Figure 2.5 - Temperature dependence of conductivity for high T [7]

Conductivity along the nonpolar axes is approximately two order of magnitude lower than the one measured along the c-axis, and this is attributed to different charge transport mechanisms.

2.4. Optical Properties

One of the most important features of $KTiOPO_4$ is the high transparency over a wide range of frequencies that allows for generation and amplification of

wavelengths going from the UV to the mid-IR region. KTP has a transparency window that goes from 350nm to 4300nm, along which it is possible to observe strong absorption due to OH⁻ anions around 2800nm and a lower transmission in the IR region due to vibrational modes of PO_4 tetrahedra and TiO_6 octahedra (figure 2.5).
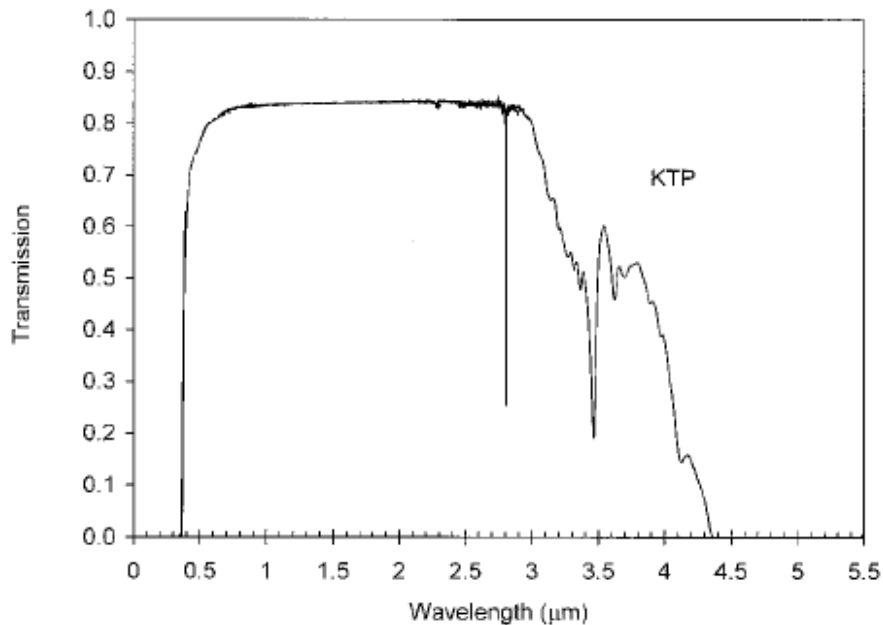
Figure 2.6 - KTP transmission window [53]

Incorporation of impurities leads to strong changes in the absorption, sometimes with beneficial effects as for the case of Cerium doping, which increase the near-UV transmission, and more often leading to the raise of absorption centres in the visible range as in the case of Pt or W impurities. It has been also observed that the presence of Fe moves the cut-off edge of the IR region to lower wavelengths. Annealing at high temperatures (between 500 and 800°C) and in different atmospheres (dry-Oxygen, Hydrogen, under vacuum) influences the absorption, but studies have led to conflicting results, without providing a definitive beneficial treatment to improve transparency.

Birefringent phase matching can't be achieved for fundamental wavelengths under 900nm because of the low birefringence of the material; this is one of the reason why much effort has been put in the fabrication of periodic poled crystals. To calculate the exact period Λ_{coh} for QPM poling it is necessary to know with high precision the refractive index experienced by the fundamental wave. Dispersion of refractive indices is well described by the Sellmeier equation:

24

$$n^2 = A + \frac{B}{1 - \left(\frac{C}{\lambda}\right)^2} - D\lambda^2 \qquad (2.3)$$

where the coefficients for the different axes are listed in table 2.1.

	A	B	C	D
n_x	2.16747	0.83733	0.04611	0.01713
n_y	2.19299	0.83547	0.04970	0.01621
n_z	2.25411	1.06543	0.05486	0.02140

Table 2.1

KTP is a positive biaxial crystal, refractive indices measured at 1064nm for the three principal directions are listed in table 2.2, together with their temperature coefficients.

	x	y	z
n	1.7400	1.7469	1.8304
dn/dT ($\cdot 10^{-5}$ °C^{-1})	1.1	1.3	1.6

Table 2.2

The nonlinear optical tensor is in the form:

$$\begin{pmatrix} 0 & 0 & 0 & 0 & d_{15} & 0 \\ 0 & 0 & 0 & d_{24} & 0 & 0 \\ d_{31} & d_{32} & d_{33} & 0 & 0 & 0 \end{pmatrix} \qquad (2.4)$$

	d_{15}	d_{24}	d_{31}	d_{32}	d_{33}
value (pm/V)	6.1	7.6	6.5	5	13.7

Table 2.3

with values of d_{ij} measured for 1064nm radiation given in table 2.3 [2]. For nonlinear optical generation it is always used the highest nonlinear coefficient, i.e. d_{33}, aligning the fundamental beam polarization with the c-axis.

2.5. KTP isomorphs

In order to improve the optical and physical properties of these nonlinear materials, many researchers have conducted studies on the compounds of the KTP family identified by the general formula MM'OXO4, where M is a monovalent element or radical, M' a tri-, tetra- or pentavalent element and X one among P, As, Si or Ge. Here we describe the main features of the isomorphs used for our experiments, namely KTA, RTP, RKTP and RTA.

2.5.1. KTA

Potassium Titanyl Arsenate sees the substitution of P for As, with a crystalline structure similar to the KTP one. The properties of this material are largely documented because of its improved optical features, which make it the most used KTP isomorph for nonlinear optical devices. The presence of a distortion of the AsO_4 tetrahedron more pronounced than the one of the PO_4 counterpart in KTP is supposed to be the cause for its higher nonlinear coefficient. The crystal can achieve second harmonic generation up to 1.6 times larger than the one obtained with KTP crystals, and shows a broader transmission spectrum going from 350 to 5300nm (figure 2.6).
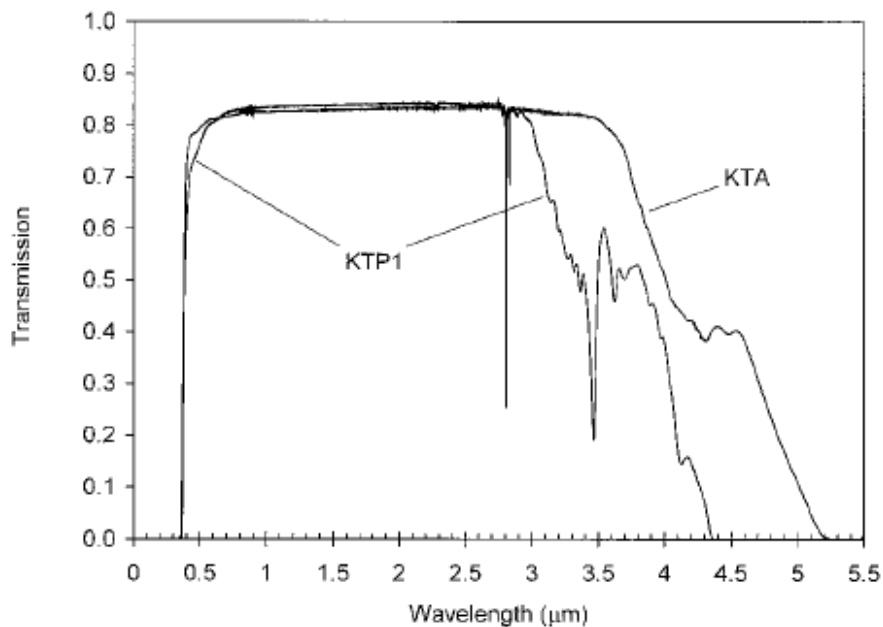
Figure 2.7 - Comparison between KTA and KTP transparency windows [53]

The material presents ferromagnetic features similar to the one encountered in KTP, with 180° domains and a second-order transition to a paramagnetic state with a Curie temperature varying over a wide range as in KTP, from 800 to 880°C depending on the growth method. Due to the lower defects concentration, ionic conductivity in KTA is approximately ten times lower than in KTP. Birefringence is also lower, which makes it adapt for applications at higher wavelengths. As well as KTP, KTA is widely used for SHG from the near-IR and for fabrication of OPOs in the mid-infrared region, exploiting the broader transparency window.

2.5.2. RTP and RKTP

After substitution of Potassium for Rubidium, Rubidium Titanyl Phosphate crystallizes in the same space group of KTP with a similar structure. There are no significant differences between the optical properties of this compound and the one of Potassium Titanyl Phosphate, such as transparency range and nonlinear coefficients ($d_{33}=17.1$); the only exception is the larger refractive indices of RTP, which results in a higher electrooptic effect. In RTP 180° ferroelectric domains have been detected, together with a second-order transition at Curie temperatures ranging between 785 and 829°C. The most important property of this isomorph, that makes it of particular interest if compared with KTP, is its lower conductivity along the c-axis due to the larger Rb atoms, which travel with more difficulty through the helical channels. The typical values for σ (10^{-9}S/cm) at room temperature are several orders of magnitude lower than the ones measured in KTP, feature that allows for an easier periodic poling of the crystal at room temperature without any risk for dielectric breakdown. It has been observed that RTP exposed to several domain-switching cycles shows constant values for coercive and internal field for every cycle, while in KTP the easier redistribution of Potassium vacancies during the multiple switching leads to a progressive decrease of these quantities [3].

Similar features are obtained in Rubidium-doped KTP, namely RKTP, a compound where Potassium is not completely substituted by Rubidium, but where it is still possible to observe a drastic decrease of conductivity. It has been shown that QPM gratings written inside RKTP with electrical periodic poling have a better quality than in KTP [5], showing excellent uniformity along the c-axis and reducing the lateral domain broadening.

2.5.3. RTA

In Rubidium Titanyl Arsenate we can find the combination of the features described in the previous paragraphs for KTA and RTP, since it shows improved optical properties as in the case of KTA, and conducting properties similar to those of RTP. The transparency window range from 350nm to 5300nm, while the distortion of the AsO_4 tetrahedron characteristic of arsenates improves the nonlinear optical performance, giving higher nonlinear coefficients d_{32} and d_{33} compared to those of KTP. The change of Potassium for Rubidium has the same consequences as in RTP, where the most important feature is again the lower

ionic conductivity, which facilitate the periodic poling process avoiding any dielectric breakdown. The ferroelectric properties are the same seen for the other crystals, the only difference is a lower Curie temperature, around 765°C. In RTA second harmonic generation has been demonstrated for both type I and type II phase matching; also tunable optical parametric oscillators have been built.

3. Reversible Damaging Processes in KTP

Crystals from the KTP family, given their high damage threshold and their excellent thermal properties, are often used for frequency conversion from high-power lasers. Strong effort has been put in studying the damage formation and the energy threshold in different conditions, where for damage it was intended a non-reversible and catastrophic fracture of the material. In table 3.1 are reported some of the threshold values for various beam parameters and growth methods (hydrothermal or flux growth).

Growth method	λ(nm)	Pulse width	Repetition rate	Damage threshold (GW/cm^2)
Flux	1064	1ns	Single shot	15
Hydrothermal	526	30ps	10Hz	30
Flux	526	30ps	10Hz	10
Hydrothermal	1064	11ns	10Hz	2-3
-	1064	30-200ns	-	15
Flux	1064	11ns	2Hz	3-3.5
Flux	532	11ns	2Hz	2.5-3
Flux	1064	8.5ns	Single shot	31
Hydrothermal	1064	30ns	Multiple shot	0.65

Table 3.1

However different reversible mechanisms causing a loss of efficiency, also addressable as damages, have been identified, in which an induced absorption for specific frequencies is observed, diminishing the amount of transmitted radiation through the crystal. This is the case of grey-tracking and of Blue Light Induced Infrared Absorption, in short BLIIRA (which is analogous to GRIIRA, caused by green light instead). The following sections give a review of the progresses in the study of these two phenomena.

3.1. Grey-Tracking

Grey-tracks have been first reported during second harmonic generation of green light from a 1064nm source, where an efficiency loss was observed during the operation, together with the formation of grey-coloured lines along the beam path (figure 3.1). These same striations were obtained during X-rays irradiation and by application of high electric fields along the c-axis. The phenomenon was attributed to the trapping of free electrons and holes generated from these highly energetic processes, which caused the formation

of colour centres and generated a strong induced absorption in the visible range.
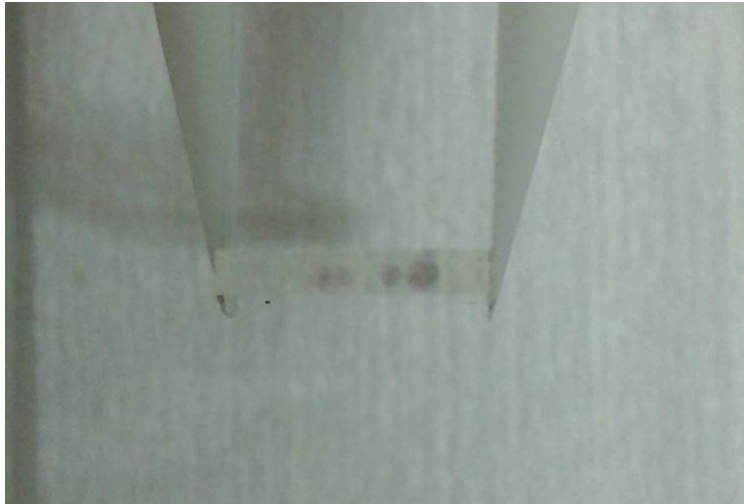
Figure 3.1 - Grey-tracks visible in transparency along the c-axis in an RTP sample

Different studies have been conducted to identify the wavelength responsible for grey-tracks in KTP, considering as possible candidates radiations at 1064, 532 and 355nm, all present during SHG process from the near IR to the visible range (they are respectively fundamental, second harmonic and non phase-matched sum frequency). The results are often conflicting, and no definitive model to describe the complete phenomenon has been given. Boulanger et al. [10] have shown that the presence of the only 532nm wavelength is sufficient for crystal grey-tracking, while the other two radiations don't contribute at all in the damaging mechanism. Other measurements report that green light can grey-track the material, but the addition of the IR component and the simultaneous presence of second harmonic and fundamental frequency gives as a result an higher induced absorption [13]. In other studies by Blachman et al. [48] colour centres have been formed with the use of the only UV radiation at 355nm.

Despite the conflicting results it has been shown by several authors [13,17,19,24] that grey-tracking and colour centres formation are nonlinear processes involving two-photon absorption, at least when dealing with wavelengths over 400nm, given the band gap of the material (3.6eV), which is transparent for radiations over 350nm. The presence of Ti^{4+}-V(O) complexes and Fe^{3+} ions inside the lattice of the crystals has been indicated as the cause for the trapping of respectively electrons and holes generated after the absorption of

high energies. The redistribution of the charge during formation and decay of the grey-track is described by [11]:

$$Fe^{3+} + h^+ \rightleftharpoons Fe^{4+}$$
$$Ti^{4+} - V(O) + e^- \rightleftharpoons Ti^{3+} - V(O) \tag{3.1}$$
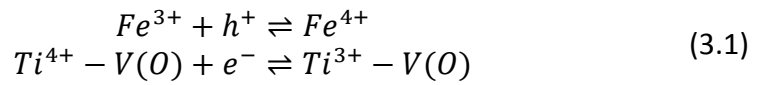
where the double arrow indicates that the damage is reversible. In this model the amount of initial defects inside the crystal, determined by the different growth methods, is strongly related to the maximum absorption induced by the grey-track, which saturates after a transient whose duration depends on the number of generated free charges. It has been observed that the formation of Fe^{3+} and Ti^{3+} produces large absorption bands in the visible range around 500nm and under 400nm [11,12]. When the damaging beam is turned off it is possible to observe a recovery of the induced absorption to lower levels which follows a double exponential decay [14].

Another model has been proposed by Mürk et al. [14] where Potassium plays a main role in the colouration of KTP. The generation of unstable pairs of Potassium vacancies and K^+ ions allows for the formation of colour centres during their lifetime of 1-10ms. Two possible recharging mechanisms have been hypothesized: a volume containing a K^+ ion captures an electron causing the formation of a Ti^{3+} centre, or in the other case holes outside the volume form oxygen colour centres. Recharging of these pairs during their lifetime is unlikely for low excitation density, so that without any exciting beam or electric field they recombine without any effect on the crystal quality. The gray tracking formation has been divided in two stages (A and B in figure 3.2): a fast rise in the induced absorption is attributed to the filling of traps deriving from native defects of the crystal (A), while for long exposure a progressive drift of the optical density is supposed to be caused by radiation-induced defects (B). A patented thermo-treatment and an addition of ions in the lattice of KTP to reduce the non-stoichiometry of the crystal resulted in a reduction of the grey-tracks formation. According to these studies there is a strong correlation between the ionic conductivity of the crystal and the damage entity, with beneficial effects deriving from a reduction of σ. Other papers exclude this hypothesis, given the data obtained from their studies [9].
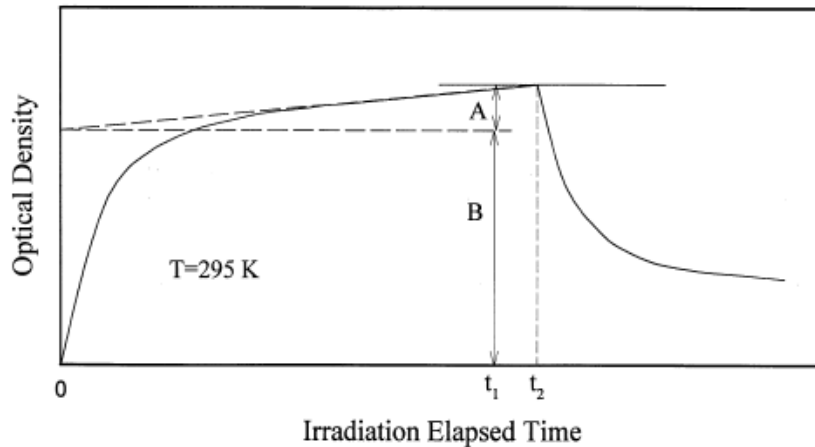
Figure 3.2 - Grey-track formation over time in Mürk model [14]

A model for grey-tracking accumulation of damages induced by pulsed sources is described by Zhang et al [22]. A multiphoton absorption process which causes the formation of Ti^{3+} and O^{2-} centres is presented. The number of centres generated by a single laser pulse is:

$$\Delta n = DF_0^m k_B T e^{-\frac{U_0 - \gamma\sigma}{k_B T}}$$ (3.2)

where D is a proportionality constant, F_0 is the peak photon flux density, m the order of multiphoton absorption, U_0 the activation energy for the damage, γ is a material parameter and σ is the induced stress. Having $U_0 > \gamma\sigma$ leads to a catastrophic damage for the crystal, so that in the simulation this case is not considered. This model allows one to simulate the growth of colour centres density over time; the results are shown in figure 3.3 where the process is depicted for different conditions, changing parameters such as the laser energy (a), frequency (b), radius (c) or the crystal temperature (d).
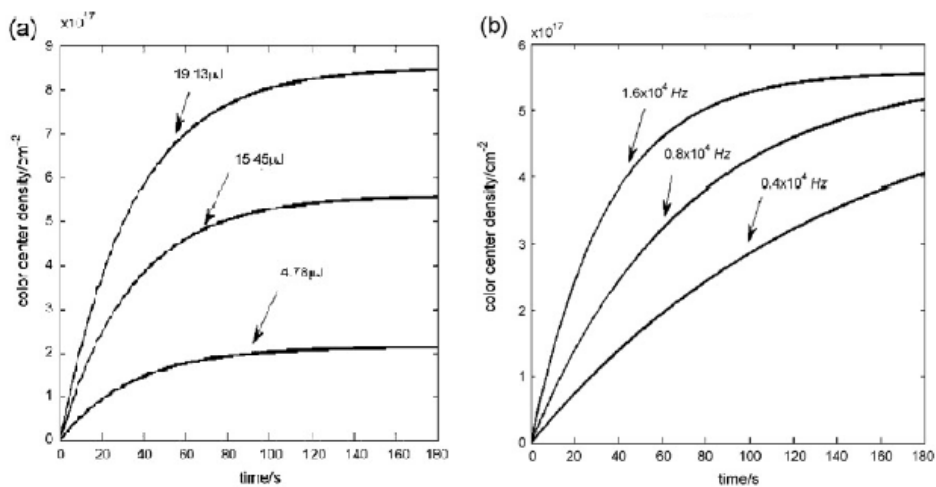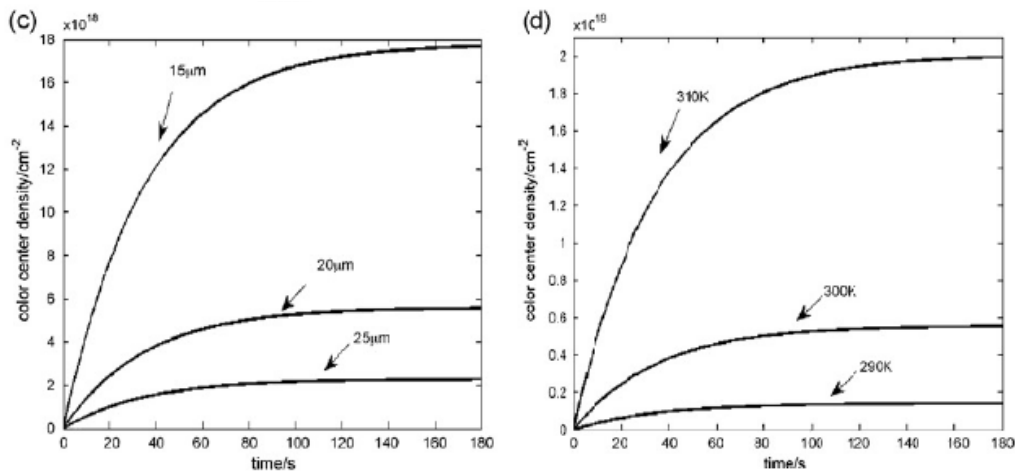
Figure 3.3 - Grey-track formation from calculation by Zhang et al. for a) different energy, b) different repetition rate, c) different radius of the damaging beam and d) different crystal temperature [22]

Several researches reported on the behaviour of gray-tracking at different temperatures [9,20], and according to each of them it is possible to observe a faster recovery from the damage at higher temperatures, together with a lower saturation level for the induced absorption. In some cases no damage has been recorded over a threshold temperature, identified for KTP as 170°C [15]. For a complete recovery from grey-tracking it is sufficient to anneal the crystals in air at temperatures over 300°C for a few hours, while annealing at higher temperature in dry-oxygen atmosphere causes an enhancement of colour centres absorption.

Grey-tracking of KTP has a strong dependency on the polarization of the damage-inducing radiation. A stronger absorption is observed for polarization parallel to the c-axis, while a much lower one has been reported for the orthogonal polarization. Studies conducted on Raman spectra of KTP before and after grey-tracking indicate that there is no substantial change in the crystalline structure, while some residual strain has been detected via synchrotron X-ray topography.

Despite some vendors have launched on the market grey-track resistant KTP (GTR KTP), this kind of crystals have shown an even higher colouration and a lower transmission in the visible range when compared to standard KTP. Slightly better performances have been reported for RKTP, which shows some resistance to gray-tracking [24].

3.2. BLIIRA

Blue Light Induced Infrared Absorption is a mechanism observed in several nonlinear crystals, including KTP, causing a loss of efficiency during second harmonic generation from the near infrared (around 800nm). The doubled frequency, which falls in the blue range, generates colour centres following the processes we have described for grey-tracking. From the levels near the edge of the bandgap, where the free charges are trapped, it is possible to have absorption of the infrared radiation to the conduction band (figure 3.4), resulting in a loss of the overall efficiency for the second harmonic generation.
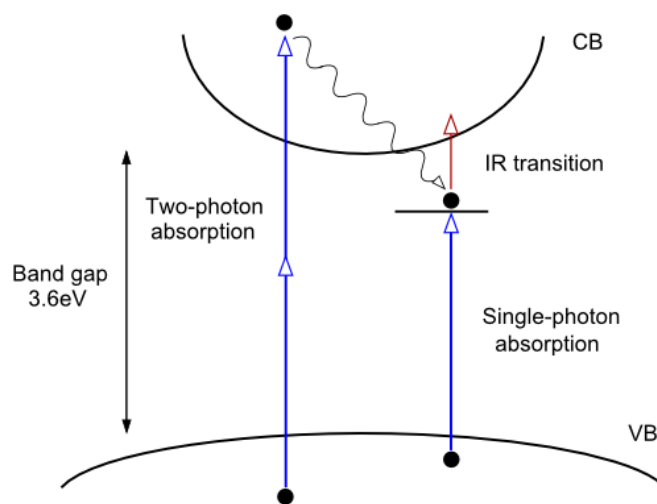
Figure 3.4 - Possible trapping mechanisms and subsequent IR absorption in nonlinear crystals

It is not clear if the traps located within the bandgap are natively present inside the band structure and populated via a single photon absorption or if a nonlinear absorption generates and populates the defects. The fact that colour centres are involved with infrared transitions is validated by the photoluminescence bands ranging from 1 to 1.8 eV detected on grey-tracked KTP crystals and attributed to transitions involving the Ti^{3+} ion. Since BLIIRA and grey-tracking are strictly related, it is possible to observe similar features for the two phenomena, such as an higher sensitivity for light polarized along the c-axis, a faster recovery from damage at higher temperatures and the complete recovery when annealing in air at temperature over 300°C.

Hirohashi et al. [19] have studied BLIIRA for exposure to 1ps pulses at 400nm in different nonlinear crystals, including KTP. They have shown that periodically poled materials undergo higher induced infrared absorption than single-domain ones (figure 3.5), and in KTP this has been related to a spatial

redistribution of K^+ and $V(K^+)$ during the domains inversion, which act as stabilizing defects for O^{2-}/O^- and Ti^{4+}/Ti^{3+} colour centres.
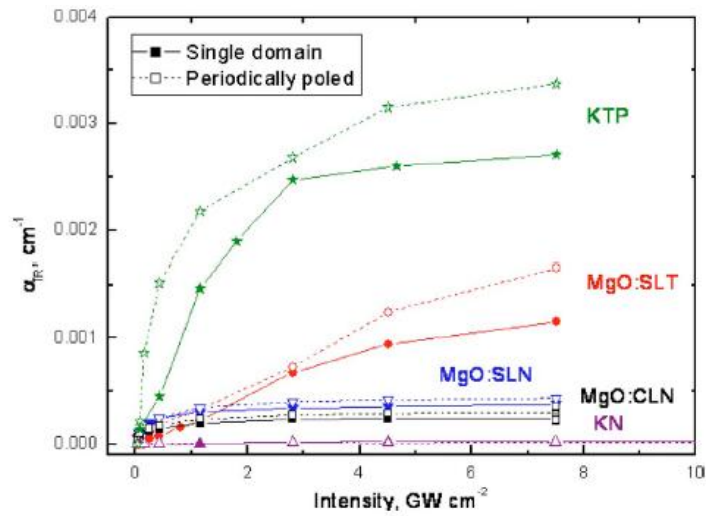
Figure 3.5 - Comparison of BLIIRA effects for different intensities of the blue beam between poled and unpoled ferroelectrics [19]

The measurements have been carried out switching on and off the damaging blue beam and observing the rise and the subsequent decay of the absorption coefficient for infrared light. KTP resulted as the crystal showing the slowest dynamics, with a damage threshold of 35MW/cm^2. The measured intrinsic absorption coefficient for 1064nm radiation was $7.6 \cdot 10^{-4}$ cm^{-1}, and after an exposure of several minutes at an intensity of 1.2GW/cm^2 it became more than 2.5 times larger than the initial value. The induced absorption increases nonlinearly with the intensity of the blue beam as depicted in figure 3.6, showing a saturation of BLIIRA in PPKTP at higher intensity than in the other nonlinear crystals.
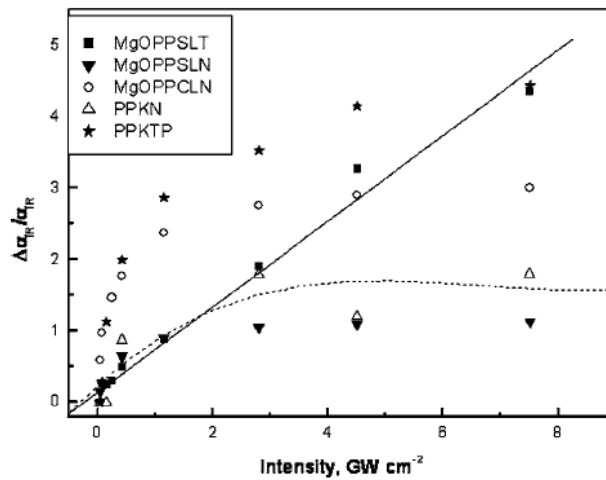
Figure 3.6 - Behaviour of BLIIRA in periodically poled ferroelectrics with increasing intensity of the damaging beam [19]

35

GRIIRA, acronym for Green Induced Infrared Absorption, is an effect analogous to BLIIRA where the absorption is induced by a beam with wavelength around 500nm. There are strong similarities between the two phenomena, so that for our purposes it is interesting to observe the results obtained by Wang et al. [18] in their studies on GRIIRA on KTP and PPKTP. The analysis on the two crystals reports an higher absorption in the poled one, with values comparable with the ones from the previous cited paper regarding BLIIRA. The decay of α_{IR} is different for poled and unpoled KTP, showing a double-exponential behaviour for the single domain crystals and a single exponential for PPKTP, which loses the fast component (figure 3.7).
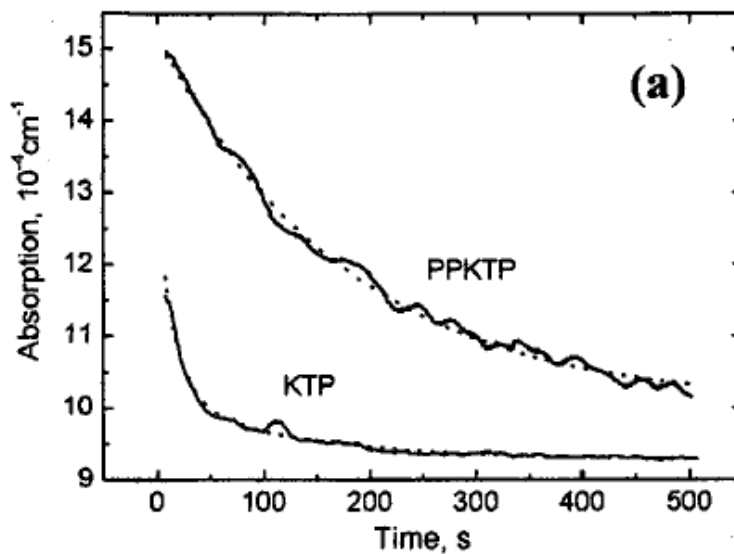
Figure 3.7 - Relaxation dynamics of GRIIRA in poled and unpoled KTP samples [18]

The periodically poled crystals were annealed before usage to avoid any residual internal strain deriving from the poling procedure. A measurement of BLIIRA on a crystal that didn't pass through the annealing step showed a completely different behaviour of α_{IR}, with the presence of an overshoot when the blue beam was switched on or off (figure 3.8). This strange feature has been related to the presence of some internal strain and consequent local piezoelectric field changing the normal trend followed by the induced absorption. After annealing at 200°C for 1 hour the effect disappeared; also after the normal relaxation of grey-tracks at ambient temperature the overshoot didn't show up again.

36
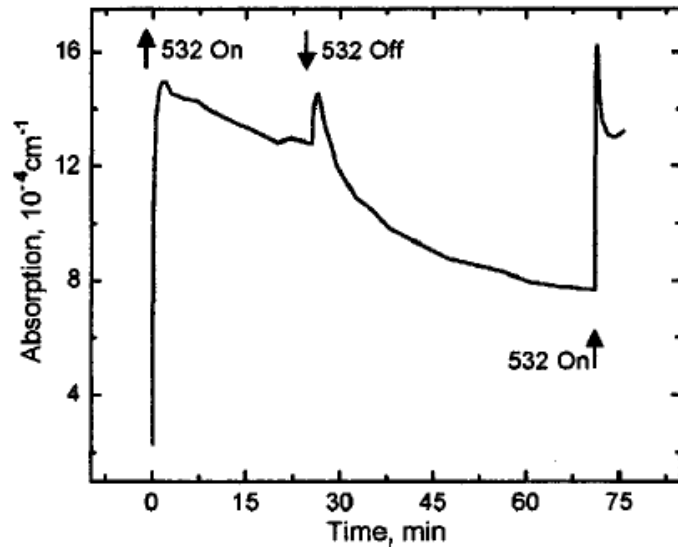
Figure 3.8 - GRIIRA dynamics in PPKTP samples which were not annealed after the poling process [18]

4. Experimental Setup

We now describe the setup used in our experiment to measure the infrared absorption coefficient of the different crystals from the KTP family. Our intent was to record the dynamics of BLIIRA over long times, and considering the high transparency of these materials for wavelengths near to 1μm we needed some technique that allowed us to measure low absorption coefficients, with a resolution on α of at least 10^{-5}cm^{-1}. We start illustrating the thermal lens method we have chosen for this purpose, passing then to the description of our complete setup. In the end we show the features of the infrared source that has been expressly built for our scope.

4.1. Thermal Lens Spectroscopy

To obtain the desired resolution for the absorption coefficient it is possible to exploit a technique that has been already adopted by Wang et al. [18] and Hirohashi et al. [19] for a similar experiment, also described extensively in literature [31,33,34,35,36,49]. It consists in a pump-probe system, where an infrared pump beam focused inside the crystal induces a thermal lens that changes the phase front of a collinear probe beam (usually a stable He-Ne laser at 633nm). The pump is chopped so that the probe beam phase is modulated at the chopping frequency because of the effect induced by the alternated thermal lens. The thermal effects are directly related to the absorbed heat from the pump power, which depends on the absorption coefficient at that specific wavelength. Once the modulated probe beam has been isolated and its intensity has been measured by a photodiode placed behind an aperture, a lock-in amplifier filters the probe component with the induced modulation. The signal coming out from the amplifier depends on the absorption coefficient that we want to measure, and the numerical study of the problem gives a simple formula that can be used to calculate it using just a reference sample with a known absorption coefficient.

The quantitative description of the thermal lens method we report here has been given by Wang. Assuming cylindrical symmetry for the whole system, we can solve the one-dimension heat conduction equation to calculate the temperature distribution inside the crystal:

$$\frac{\partial^2 T}{\partial r^2} + \frac{1}{r}\frac{\partial T}{\partial r} + \frac{Q(r)}{k} = 0 \tag{4.1}$$

where k is the heat conductivity of the material, $Q(r) \approx \alpha I_0(r)$ and $I_0(r)$ is the pump beam intensity. The boundary condition is given considering a constant temperature at the edges of the crystal $T(r_b, z)$ and makes it possible to obtain a solution and to calculate $\Delta T(r,z) = T(r,z) - T(r_b, z)$:

$$\Delta T(r,z) = \frac{\alpha P e^{-\alpha z}}{4\pi k}\left[\ln\left(\frac{r_b^2}{r^2}\right) + E_1\left(\frac{2r_b^2}{\omega_p^2}\right) - E_1\left(\frac{2r^2}{\omega_p^2}\right)\right] \tag{4.2}$$

Here ω_p is the pump beam radius and E_1 represents the exponential integral function. Considering the integrated contribution along the whole length L of the crystal, the probe passing through it acquires a phase profile:

$$\Delta\varphi(r) = 2\pi(T(r) - T(0))\frac{L}{\lambda}\frac{dn}{dT} \tag{4.3}$$

Then the probe is isolated with a dichroic mirror from the pump, while a lens projects on the Fourier plane a field amplitude proportional to the spatial Fourier transform of the beam, which contains the information on the induced phase profile. Next the spatial distribution of the voltage signal on this plane, measurable with a photodetector, is calculated as:

$$U(r) = (P_p(r)|_{\Delta\varphi=0} - P_p(r))\eta R\gamma \tag{4.4}$$

where γ is the probe attenuation factor, η is the p-i-n detector responsivity, R is the load resistance of the lock-in amplifier and in the parenthesis we calculate the difference between the power detected without any phase distortion and with the presence of thermal lens. In figure 4.1 it is reported the simulated voltage signal plotted against the radial coordinate for different absorption coefficients.
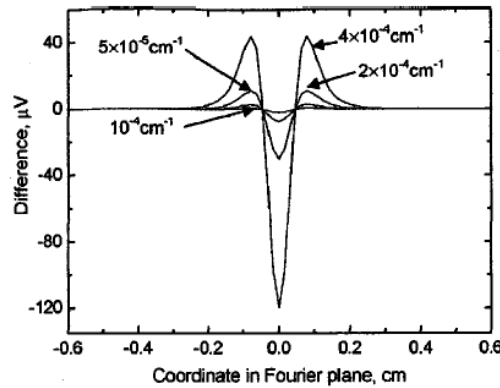
Figure 4.1 - Voltage signal intensity calculated along the radial coordinate of the Fourier plane [18]

The evaluation of the probe noise shows that, even if for $r=0$ we have the higher voltage signal, the centre of the beam is not a suitable position where to place the aperture. The higher signal to noise ratio is obtained for a value of r between 1 and 2mm (figure 4.2).
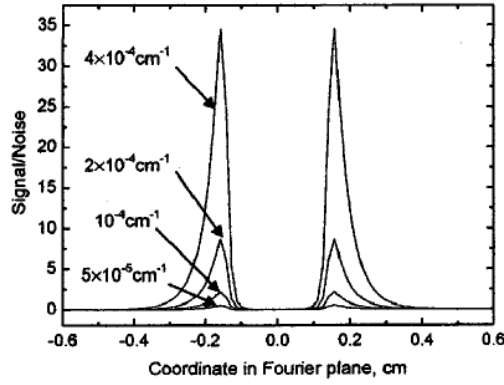
Figure 4.2 - Voltage signal intensity calculated considering the probe beam intensity noise [18]

The measurement of the signal coming from a reference sample with known characteristics allows for the calculation of the absorption coefficient of the material we are studying using the following equation:

$$\alpha_s = \alpha_{ref} \sqrt{\frac{S_s}{S_{ref}} \frac{\frac{dn}{dT}|_{ref} k_s L_{ref}}{\frac{dn}{dT}|_s k_{ref} L_s}} \qquad (4.5)$$

here S is the voltage signal from the lock-in amplifier, $\frac{dn}{dT}$ is the derivative of the refractive index with respect to temperature, k is the thermal conductivity and L is the crystal length. The subscript $"s"$ refers to the quantities of the sample under study, while $"ref"$ is related to the reference sample.

4.2. Measurement Setup

Our goal was to continuously measure the absorption coefficient before, during and after the illumination with blue light. We used three laser sources: a He-Ne probe operating at 632.8nm, a continuous wave Yb:KYW solid state laser as infrared pump at 1.04μm and a picosecond Ti:Sapphire regenerative amplifier generating pulses at 800nm with a repetition rate of 1kHz. The 800nm radiation was passing through a BBO crystal generating second harmonic at 400nm, so that we could use it as a blue pulsed source to induce BLIIRA. The three beams were reflected or transmitted by dichroic mirrors (DM1 and DM2) in such a way that they passed collinearly aligned through the crystal as

depicted in figure 4.3. The pump and the blue beam were polarized along the polar axis of the crystals, i.e. perpendicularly to the optical table. This condition simulated what normally happens during second harmonic generation, where both the fundamental and the doubled frequency are polarized along the c-axis. A system of lenses was used to focalize the pump and the probe in the centre of the crystal, with a beam waist of respectively 50 and 150μm, while the 400nm beam passed through it collimated with a radius of 350μm.
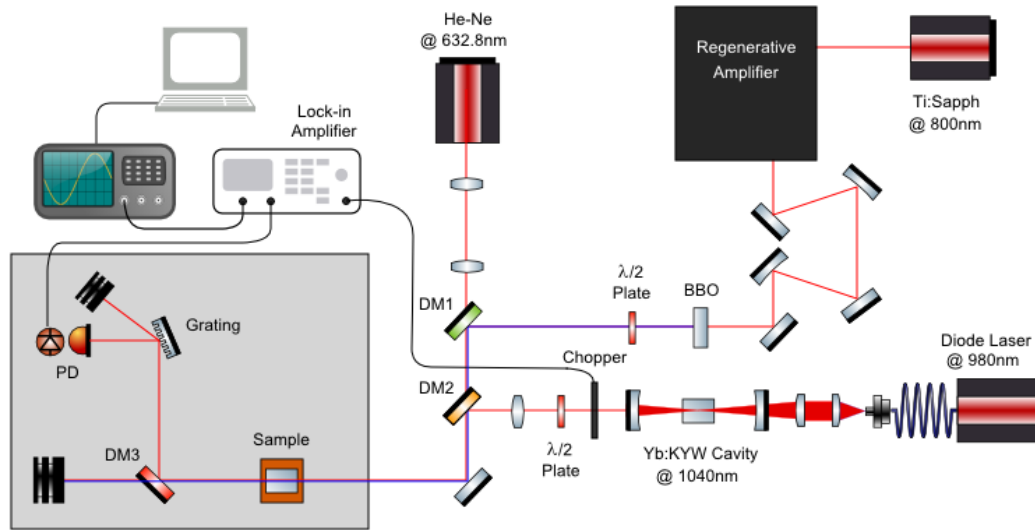
Figure 4.3 - Setup scheme

The dichroic mirror DM3 isolated the probe beam from the others, while a lens mounted in a 2f configuration performed its Fourier transform, projecting the Fraunhofer diffraction pattern on the aperture plane, behind which a photodiode collected the passing light. Behind the lens a diffraction grating further separated the He-Ne radiation from the other residual wavelengths weakly reflected by DM3. The chopper modulating the pump amplitude at 20Hz was connected to the lock-in amplifier in order to provide in real time the lock-in frequency and to extract from the photodiode signal the only component of the probe modified by the alternated thermal lens. The amplified signal was sent then to an oscilloscope to visualize its dynamics and to record it with the help of dedicated computer software. It is important to underline that the signal extracted by the lock-in amplifier was very weak (a few microvolts) and submerged by noise. To definitively eliminate any residual scattered pump and blue radiation we mounted a cylindrical enclosure onto the photodiode sensor containing an OG550 filter and two BG19 filters, placing it behind the aperture.

42

The crystals cuts were all parallel to the crystallographic axes, with a sample size of 10mm in a, 5mm in b and 1mm in c (figure 4.4a). The end faces were polished in the same batch in order to present the same surface to the incoming beams and avoid different back-reflections changing from a crystal to another, and allowing for a later comparison between the gathered data. During the measurement the crystal was housed on a copper holder whose temperature was regulated by a p-i-d controller with the use of a Peltier cell and a thermocouple (figure 4.4b). This way it was possible to establish approximately constant boundary conditions on $T(r_b,z)$ and to measure BLIIRA for different crystal temperatures.
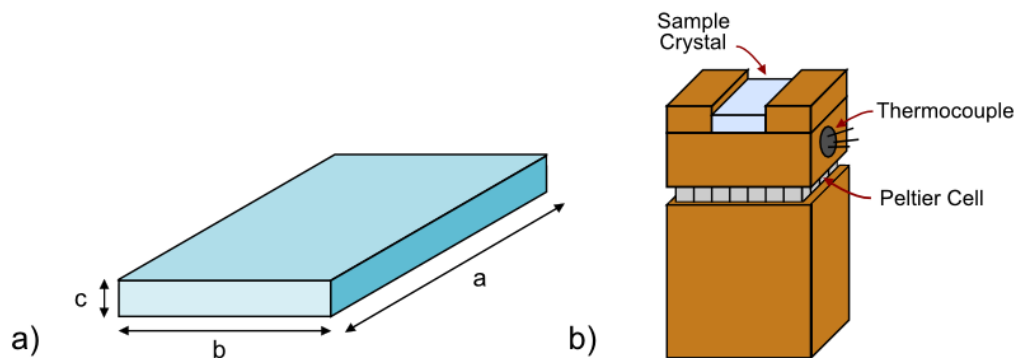
Figure 4.4 - a) crystal cuts and b) copper sample holder with thermocouple and Peltier cell for temperature control

Given the high number of degrees of freedom that we could change, such as the position of the pump and probe focuses, of the filters, of the aperture, or also the various possible settings for the lock-in amplifier (sensitivity, reserve and time constant) the initial configuration leading to an operative system was complex and time consuming. To actually produce and successfully isolate the thermal lens signal we proceeded at first with some BK7 long samples, in order to have a stronger absorption than the one in KTP (around 10^{-3}cm^{-1} instead of 10^{-5}-10^{-4}cm^{-1}) and an higher signal easier to detect. We had to pay particular attention to the residual pump beam since, given its 20Hz modulation, in case of detection on the photodiode it would have been filtered by the amplifier and mistaken as the wanted signal. Once the actual signal was isolated we built a box containing the terminal part of the setup to avoid any movement of the dust near the crystal and along the beams path after the thermal modulation. This increased the signal stability and allowed for the acquisition of data over long time.

4.3. Pump Source Characterization

We built the infrared pump source using a simple linear cavity where a 5% Ytterbium-doped Potassium Yttrium Tungstate crystal (in short Yb:KYW) was pumped by a diode laser at 980nm, generating coherent radiation around 1,04μm. The cavity is represented schematically in figure 4.5. The meniscus lens (EFL=40mm) collimated the pump beam coming out from a fiber with diameter d=100mm and NA=0.22, while the biconvex lens (f=50mm) focused it inside the active medium. The first cavity mirror was coated with an HR layer for the oscillating frequency (1020-1200nm) on the curved surface, while on the flat one it was deposited an AR coating for the pump wavelength (800-1000nm). The the output coupler had a partially reflective coating transmitting 95% of the oscillating frequency (1000-1150nm). The radius of curvature of both mirrors was r=50mm.
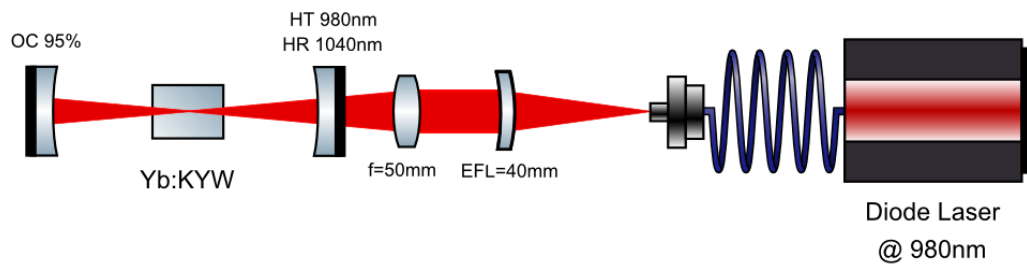
Figure 4.5 - Scheme of the Yb:KYW cavity operating at 1040nm pumped by a diode laser

The cavity was built with the help of a software simulating the beam radius dimension during propagation in an optical systems. We made sure that inside the active medium the pump was focused with a waist not larger than the radius of the cavity mode. This way it was possible to exploit the whole volume where we reached the condition of population inversion induced by the pump.
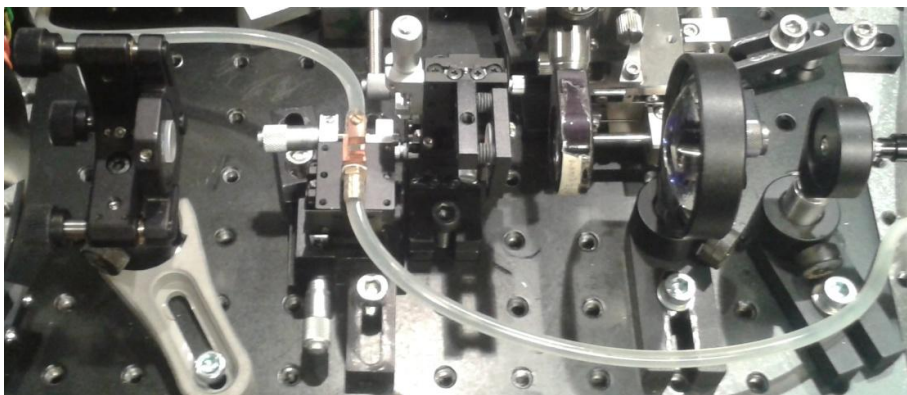
Figure 4.6 - Picture of the actual Yb:KYW cavity
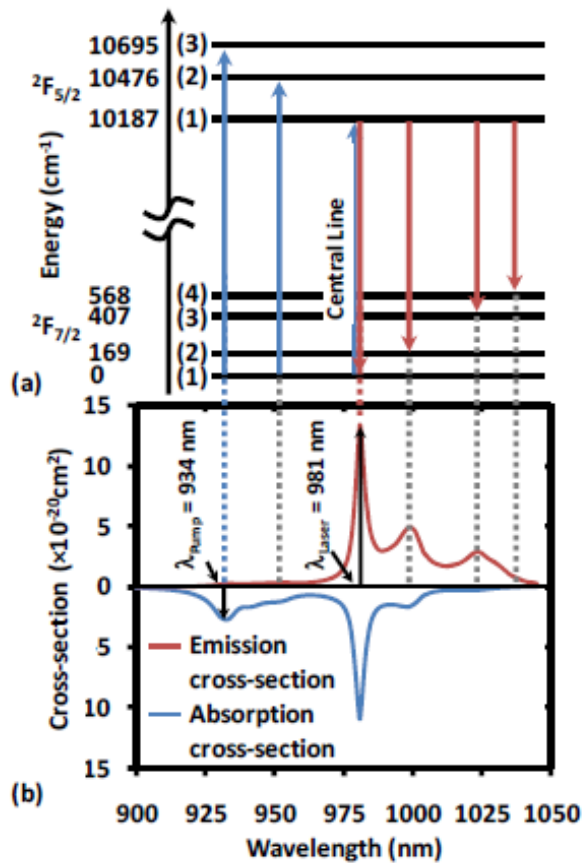
Figure 4.7 - Energy levels of Yb in a KYW matrix involved in absorption and emission processes

Yb:KY(WO$_4$)$_2$, or Yb:KYW, is an active medium based on the emission of Ytterbium ions acting as dopants in a tungstate crystal. It exhibits a peculiar quasi-three level behaviour between states belonging to the fine structures of the levels $^2F_{5/2}$ and $^2F_{7/2}$ (figure 4.6), which are split by the Stark effect induced by the glass matrix. The use of this material for high-efficiency lasers has been demonstrated in different papers [50,51], and one of the reason for this is the low quantum defect of the reemission process. In the following sections we present the measurements done to characterize our laser.

4.3.1. Output Power

The curve in figure 4.7 describes the relation between the output power of the cavity and the diode pump power. It is possible to observe a good conversion efficiency, around 33.6%, in the first linear part of the plot, while for an input power over 17W the slope of the curve decreases progressively. The value of the threshold pump power necessary to overcome cavity losses is around 2.4W.
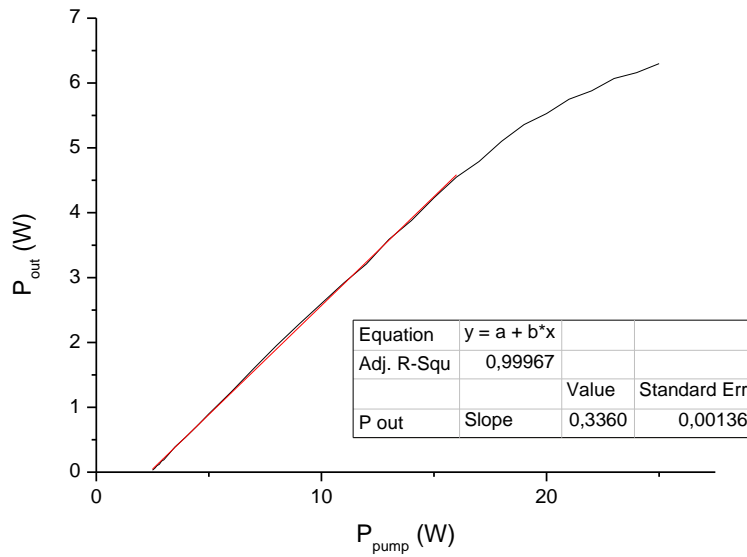
Figure 4.8 - Yb:KYW cavity output power plotted against the pump power. Linear fit (red line) showing a slope efficiency of 0.336 for pump power between 0 and 17W

The decrease in slope efficiency was accompanied by a distortion of the circular shape of the beam observable by the naked eye, and probably due to the stronger thermal lens induced inside the active medium.

4.3.2. Beam Waist and M^2

Given the hypothesis on which the thermal lens spectroscopy method is based on, in our experiment it was important to maintain a cylindrical symmetry, starting from the shape of the pump and probe beams. As a probe we used a commercial He-Ne laser, well known for its good TEM_{00} Gaussian mode, so we decided to measure just the beam radius of the Yb:KYW pump source with the knife edge technique to evaluate its circularity.

The beam radius of a Gaussian beams during propagation along z direction is described by the equation:

$$\omega(z) = \omega_0 \sqrt{1 + \left(\frac{\lambda z}{\pi \omega_0^2}\right)^2} \qquad (4.6)$$

where ω_0 is the beam waist, i.e. the minimum radius. Laser beams are not pure Gaussian beams since more often they are composed by multiple transversal modes. In this case the study of the beam radius dimension (now indicated as

W) along z can be used to calculate the M^2 factor, defined for values larger than 1 and obtained by fitting the data in the equation:

$$W(z) = W_0 \sqrt{1 + \left(M^2 \frac{\lambda z}{\pi W_0^2}\right)^2} \tag{4.7}$$

This is a good indicator of the beam quality, intended as the vicinity to a perfectly circular shaped TEM$_{00}$ mode, obtained for $M^2=1$. The higher the M^2 value, the higher the number of transversal Hermite-Gaussian modes oscillating in the cavity. The measurement of the beam radius is performed with the simple knife edge technique, adopting just a power meter and a blade mounted on a translational stage. The total power of the beam is calculated integrating the Gaussian distribution of the intensity over the two transversal directions x and y:

$$P_{tot} = I_0 \int_{-\infty}^{+\infty} e^{-2\frac{x^2}{\omega^2}} dx \int_{-\infty}^{+\infty} e^{-2\frac{y^2}{\omega^2}} dy = \frac{1}{2} I_0 \omega^2 \pi \tag{4.8}$$

If part of the beam is blocked along the y direction, the second integral has a superior limit Y and the power is calculated as:

$$\begin{aligned} P_{tot} &= I_0 \int_{-\infty}^{+\infty} e^{-2\frac{x^2}{\omega^2}} dx \int_{-\infty}^{Y} e^{-2\frac{y^2}{\omega^2}} dy \\ &= \frac{1}{4} I_0 \omega^2 \pi \left(1 + erf\left(\frac{\sqrt{2}Y}{\omega}\right)\right) \end{aligned} \tag{4.9}$$

where $erf(x)$ is defined as:

$$erf(x) = \frac{2}{\sqrt{\pi}} \int_0^x e^{-t^2} dt \tag{4.10}$$

Evaluating the ratio between equations (4.9) and (4.8) it is easy to calculate that for $Y=\omega/2$ and $Y=-\omega/2$ the percentage of transmitted power is respectively 84% and 16% of the total. The blade mounted on the translational stage is moved along the y direction (figure 4.8) until the power meter indicates the 84% of the total power. It is then translated to the position where the power decreases to 16% and the distance between these two points corresponds to the beam radius.
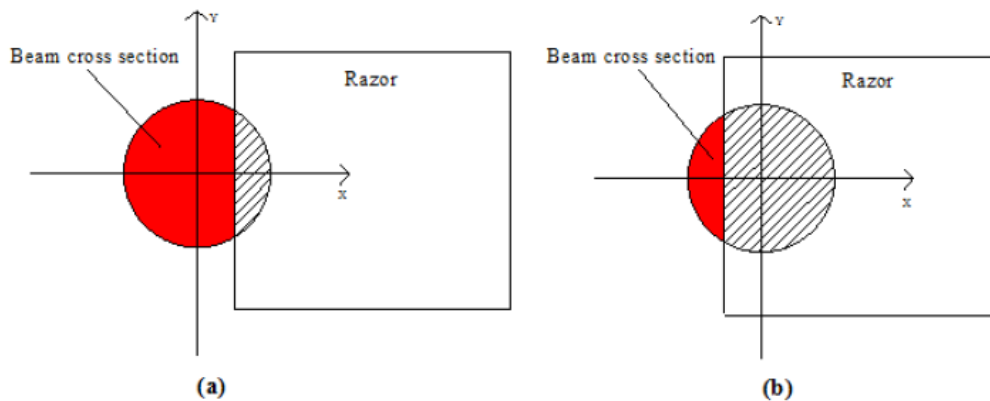
Figure 4.9 - Application of the knife edge technique and cutting of the beam to a) 16% and b) 84% of the transmitted power [27]

This measurement is then repeated for several points along the propagation direction of the beam, mounting the system on a rail moving along z. The procedure is equivalent for the measurement of the radius along the transversal x axis. For a good fit of the beam radius plotted against the z coordinate with equation (4.7) it is necessary to acquire points from both inside and outside the Rayleigh range, which is defined as the portion of space before and after a distance from the beam waist equal to the Rayleigh length, i.e.:

$$Z_R = \frac{\pi \omega_0^2}{\lambda} \qquad (4.11)$$
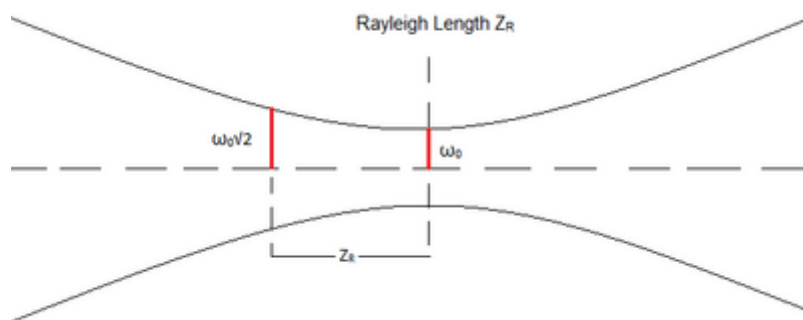
Figure 4.10 - Rayleigh length in a Gaussian beam

The curves of figure 4.9 show the values of the beam radii measured along the two transversal directions plotted against z. From the fits we obtained an M^2 value of 1, and the almost identical dimensions of the radii in the x and y directions along the propagation coordinate indicated a very low beam ellipticity. This meant that we could consider the laser as oscillating on a single TEM$_{00}$ mode and a good Gaussian beam travelling through our crystals, validating our hypothesis of cylindrical symmetry.

Equation	$w = w0*sqrt(1+((M2*l*(z-z0))/(pi*(w0)^2))^2)$		
Adj. R-Square	0,99632		
		Value	Standard Erro
	w0	0,04563	0,0019
w\-(x)	z0	16,65227	0,16168
	M2	1	0,03908

Equation	$w = w0*sqrt(1+((M2*l*(z-z0))/(pi*(w0)^2))^2)$		
Adj. R-Square	0,99281		
		Value	Standard Error
	w0	0,04744	0,00244
w\-(y)	z0	16,0321	0,22544
	M2	1	0,04806
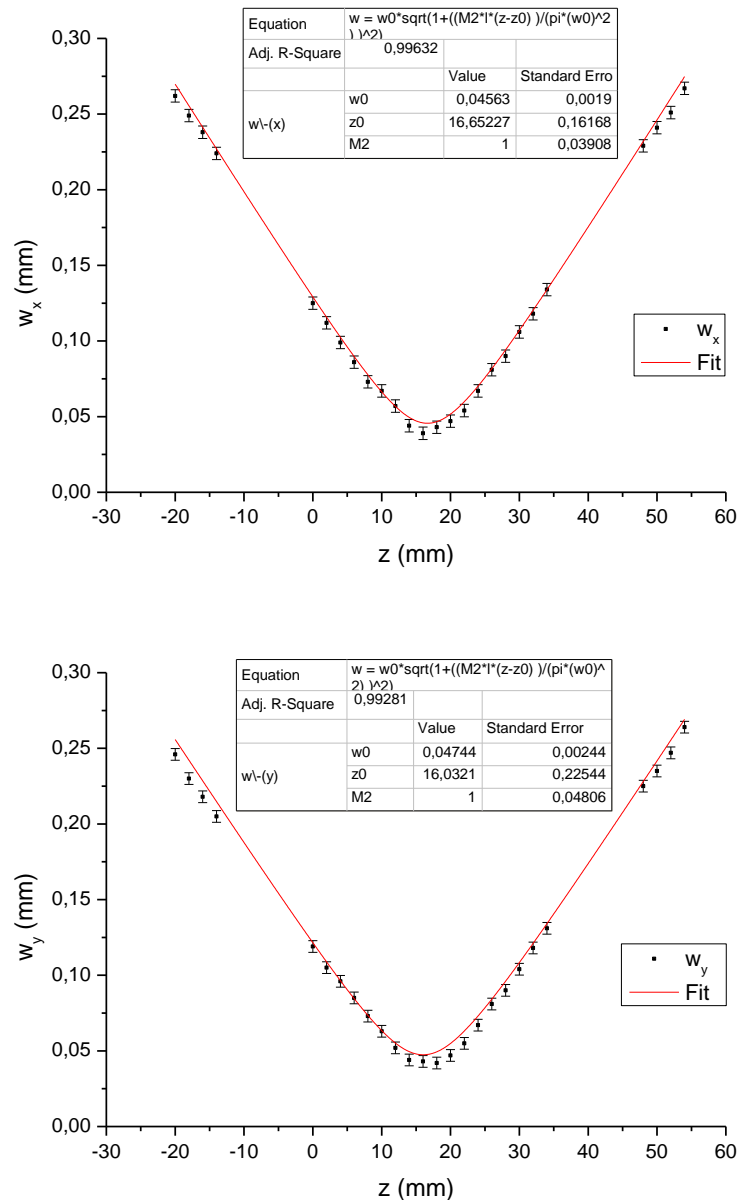
Figure 4.11 - Fit of the beam waist measurements acquired along the x and y direction

4.3.3. Frequency Spectrum

We performed a series of measurements with a spectrometer on the laser beam in order to obtain the beam spectrum for different pump powers. The curves are shown in figure 4.10. As we expected from a quasi-three level laser the central frequency shifted to higher wavelengths for higher pump powers, reaching the maximum value of 1045nm for a diode output power of 20W. This can be explained with an increase of temperature inducing a higher population density for the lower laser levels in the fine Stark structure of the state $^2F_{7/2}$,

which causes an emission from the excited state to a lower one with a progressively higher energy. Thus the energy difference between the lasing states becomes lower and the wavelength of the emitted photon results longer.
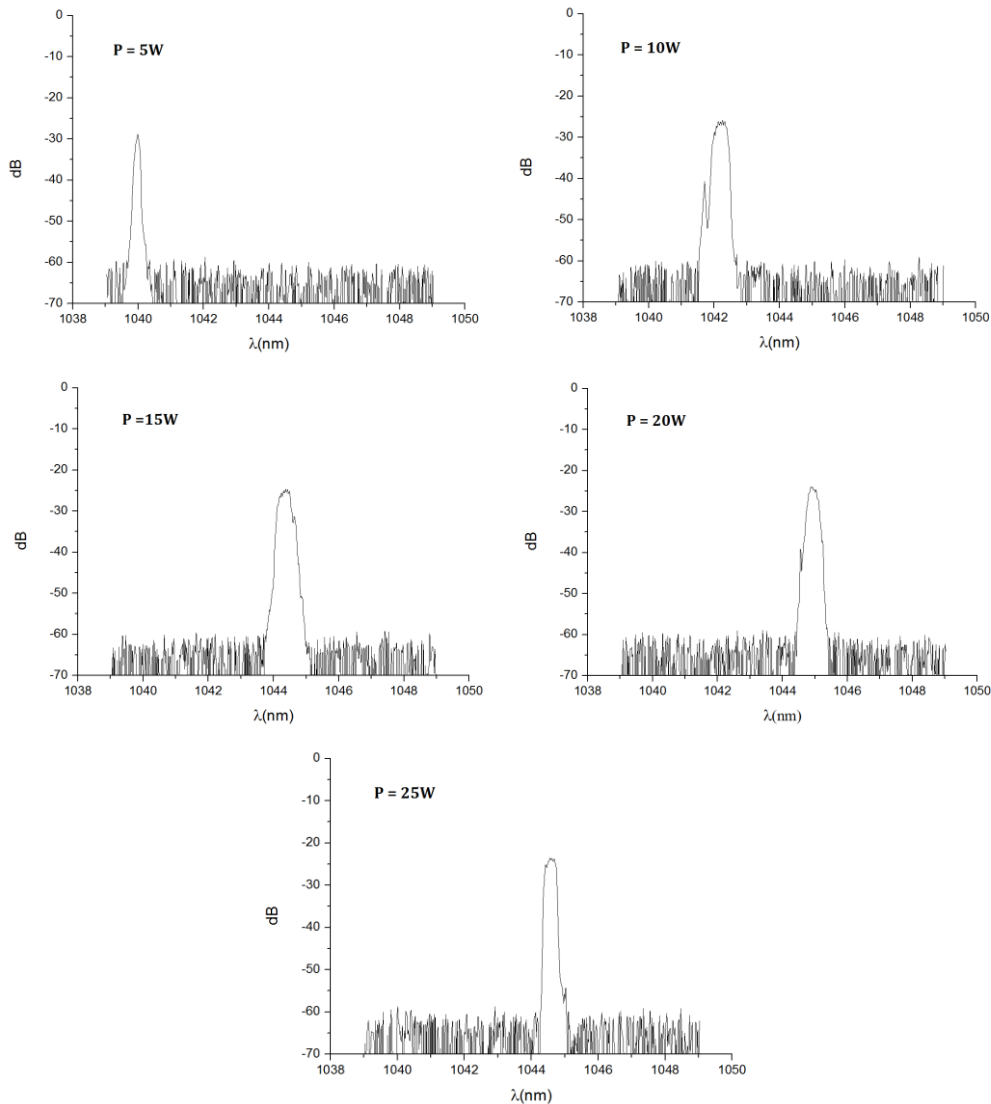
Figure 4.12 - Output spectrum at 5, 10, 15, 20 and 25W of pump power

The spectra were quite broad in all cases, and during the measurements it was possible to observe a strong competition between modes, resulting in a continuous shift of the peaks in the spectrum. For our purposes, we didn't need any single-frequency source, since it is reasonable to consider the same induced absorption for both narrow and broad spectra, at least within the range of a few nanometers from the central wavelength.

5. Data Collection and Analysis

To achieve a good level of familiarity with the setup we used at first some poor quality crystals from the KTP family, together with BK7 glasses to use as reference samples. With the practice acquired from these measurements we maximized the signal to noise ratio through optimization of the various degrees of freedom present in our system. Therefore, observing the behaviour of BLIIRA, we defined the procedure to follow for the measurements on our batch, which was composed by:

- Two KTP crystals, respectively with high conductivity and low conductivity from the same vendor
- Two high conductivity RKTP crystals and two low conductivity RKTP crystals, all from the same vendor
- Three high conductivity KTA crystals from different vendors and one low conductivity KTA crystal
- Two RTP crystals from different vendors
- One RTA crystal

The measurements were performed on a periodically poled area in all cases except for RTA, which was a single domain crystal. The period chosen for the poled crystals was not matched for SHG with any wavelength used in the experiment. BK7 was chosen as a reference sample because of its well known characteristics. In table 5.1 are listed the thermal conductivity and the temperature derivative of the refractive index for all of the materials; the absorption coefficient of BK7 at 1040nm is $\alpha_{IR}=1{,}213\cdot10^{-3}\text{cm}^{-1}$.

	BK7	KTP	RKTP	KTA	RTP	RTA
dn/dT (10^{-6} K^{-1})	0,984	11	11	11	5,6	5,6
κ (W/mK)	1,1	2	2	1,8	3	1,6

Table 5.1

These are used in equation (4.5) to calculate the absorption coefficient for each sample under study, given the reference signal acquired from BK7 and the signal recorded during BLIIRA, as we explained in chapter 4. We performed different experiments, first measuring BLIIRA for all of the crystals in the same conditions, then focusing on the damage accumulation in KTP for repeated exposure. After that we choose one crystal for each isomorph type and we

observed the induced absorption at different temperatures and blue pulse lengths. In the end we studied BLIIRA in KTA and KTP for different average power of the damaging beam. After each of these measurements we annealed the crystals in air at 250°C for about 15 hours in order to have a complete recovery from the grey-tracking.

5.1. BLIIRA in KTP Isomorphs

The first measurements were performed on all of the 13 crystals we had. Our goal was to evaluate differences among samples from different vendors and with different conductivity. We fixed the temperature of the copper holder at 25°C, setting the following specifications for our sources:

- Damage-inducing pulses at 400nm with a duration of 30ps. Average power of the incident beam of 3mW
- Yb:KYW pump laser at 1043nm operating in a CW regime with an output power of 1.8W, chopped with a 50% duty cycle resulting in an average incident power of 0.9W
- He-Ne probe laser operating at 632.8nm with an incident power of 3.9mW

The acquisition of these data was performed over several days, and a standard procedure was defined to gather comparable measurements. At the beginning, after switching on the system and waiting for its stabilization, we proceeded measuring the signal from the BK7 sample, which was considered as a stable reference for the following measurements. Then the crystal sample took the place of the reference glass and its absorption coefficient was measured using the pump-probe system without the presence of any damaging beam. This step was necessary because the acquisition of the signal for higher induced absorption required a lower sensitivity of the lock-in amplifier, which wouldn't have been sufficient for the detection of the intrinsic absorption coefficient. After these preliminary steps it was possible to proceed recording the BLIIRA dynamics. The crystal was exposed for 50 minutes to the blue pulses, then the beam was blocked and the relaxation of BLIIRA was observed again for 50 minutes. In one crystal per type we decided to repeat this procedure with another 15 minutes of exposure and 30 minutes of relaxation to observe if there was any detrimental effect and if the system showed any memory of the previous induced damage. In all cases the dynamics of the rising edge were

masked by the integration performed by the lock-in amplifier over a time of 300ms, while the slow decay was fitted with a double exponential expression:

$$\alpha = \alpha_0 + A_1 e^{-\frac{(t-t_0)}{\tau_1}} + A_2 e^{-\frac{(t-t_0)}{\tau_2}} \tag{5.1}$$

Here a part of the damage, consisting in a residual baseline α_0, is considered as permanent because of its long decay time constant. The next sections present the gathered data.

5.1.1. KTP

The two curves of figure 5.1 represent the BLIIRA dynamics for high conductive and low conductive KTP, while in table 5.2 are specified the measured intrinsic absorption of the crystals and the parameters regarding BLIIRA relaxation.
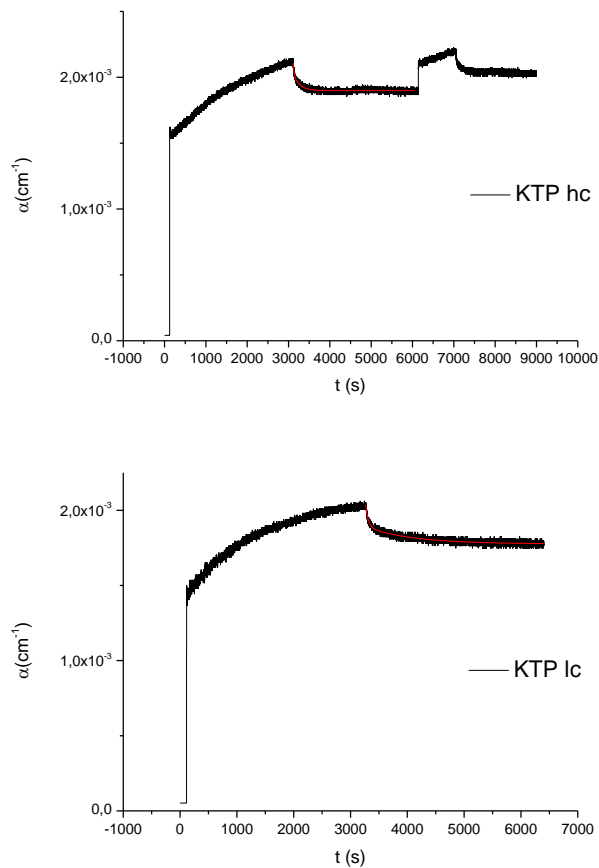

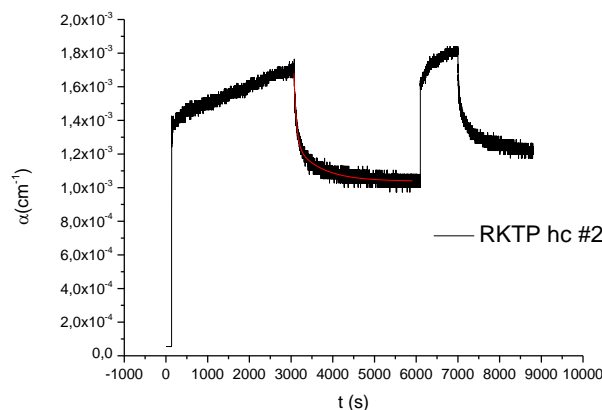Figure 5.1 - BLIIRA in high- and low-conductive KTP

	α_{start} (cm^{-1})	A_1	τ_1 (s)	A_2	τ_2 (s)	α_0 (cm^{-1})
KTP hc	$4,11 \cdot 10^{-5}$	$1,35 \cdot 10^{-4}$	160	$1,30 \cdot 10^{-4}$	21	$1,90 \cdot 10^{-3}$
KTP lc	$5,20 \cdot 10^{-5}$	$1,14 \cdot 10^{-4}$	835	$1,85 \cdot 10^{-4}$	48	$1,78 \cdot 10^{-3}$

Table 5.2

The table shows much longer decay time constants for the low conductivity sample, and a comparable baseline absorption value for the two crystals after relaxation. The intrinsic absorption coefficient resulted similar in both cases and lower than the one reported in other works [18,19], however this might be due to different growth methods or crystal qualities. The fast rise of BLIIRA is followed by a slower drift to higher values of α with dynamics that don't seem influenced by conductivity. The levels of induced absorption are approximately the same for the two crystals, starting from 1,5 - 1,6·10^{-3}cm^{-1} and reaching values of 2,0 - 2,1·10^{-3}cm^{-1} after 50 minutes. During the study of the memory effect we can see that shining again blue light brings back the absorption coefficient to the same level it had when the relaxation started.

5.1.2. RKTP

Doping of KTP with Rubidium reduces significantly the induced absorption levels, which in all cases range between 1,4 - 1,6·10^{-3}cm^{-1} as shown in figure 5.2. The damage with slow decay dynamics modelled as a baseline is lower than in KTP and similar for all of the four RKTP samples, as well as the intrinsic absorption values, comparable with the ones for KTP. Table 5.3 lists the time constants of relaxation, that in this case can't be related so clearly with conductivity, since for the HC sample #7 τ_1 results higher than in the LC sample #8, while the situation is reversed for HC sample #2 and LC sample #1. The fast time constant τ_2 presents comparable values for all of the samples. The lower contribute to relaxation given by the higher conductivity might be related to the presence of Rubidium, inhibiting the redistribution of Potassium ions and vacancies.
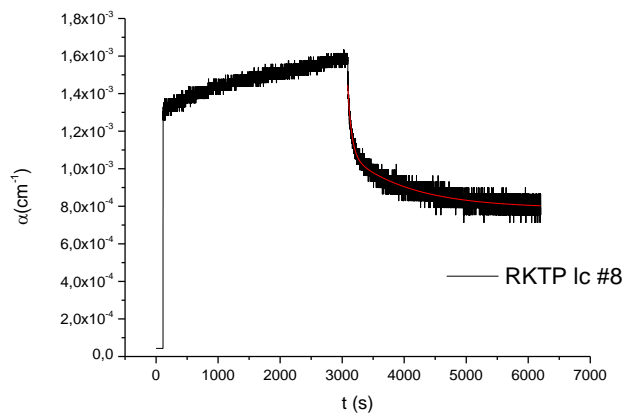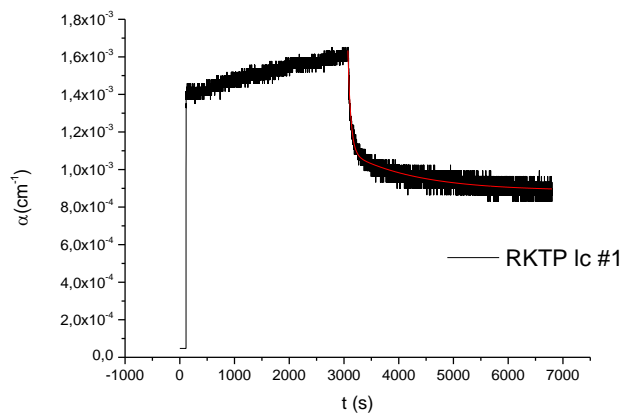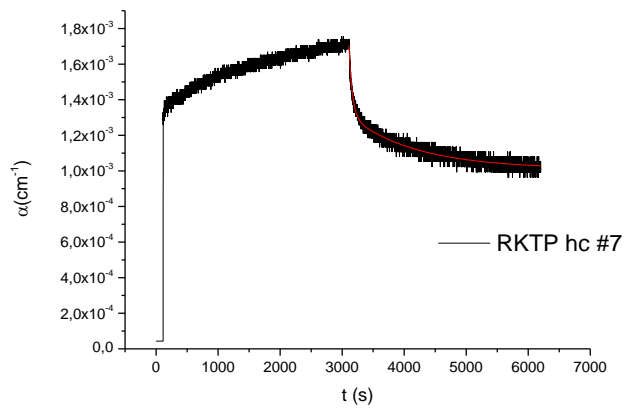
Figure 5.2 - BLIIRA in different samples of high- and low-conductive RKTP

	α_{start} (cm^{-1})	A_1	τ_1 (s)	A_2	τ_2 (s)	α_0 (cm^{-1})
RKTP hc #2	$5,52 \cdot 10^{-5}$	$2,26 \cdot 10^{-4}$	630	$6,79 \cdot 10^{-4}$	61	$1,04 \cdot 10^{-3}$
RKTP hc #7	$4,33 \cdot 10^{-5}$	$3,05 \cdot 10^{-4}$	1072	$5,75 \cdot 10^{-4}$	55	$1,01 \cdot 10^{-3}$
RKTP lc #1	$4,74 \cdot 10^{-5}$	$2,11 \cdot 10^{-4}$	1242	$1,14 \cdot 10^{-4}$	54	$8,87 \cdot 10^{-4}$
RKTP lc #8	$4,33 \cdot 10^{-5}$	$2,92 \cdot 10^{-4}$	1000	$5,89 \cdot 10^{-4}$	63	$7,90 \cdot 10^{-4}$

Table 5.3

The same drift we observed in KTP is present here, but with a lower steepness. The memory test run for the HC RKTP #2 sample shows that also in this case the drift starts over from where it stopped before relaxation.

5.1.3. KTA

The recorded measurements for KTA are shown in figure 5.3. Here the curves have different trends, with the LC KTA and the crystal from Vendor #1 showing again a positive drift (with an overshoot in the latter during the first fast rise), and the samples from Vendor #2 and the HC KTA presenting a drift with a negative slope. In these latter cases we see an overshoot after the blue beam is switched on, followed by a jump to higher values when the damage-inducing beam is switched off, with the subsequent relaxation starting from a higher point than the one reached after the drift. KTA from Vendor #1 showed no changes in BLIIRA dynamics after a second stage of illumination testing any possible memory effect from the previous exposure.
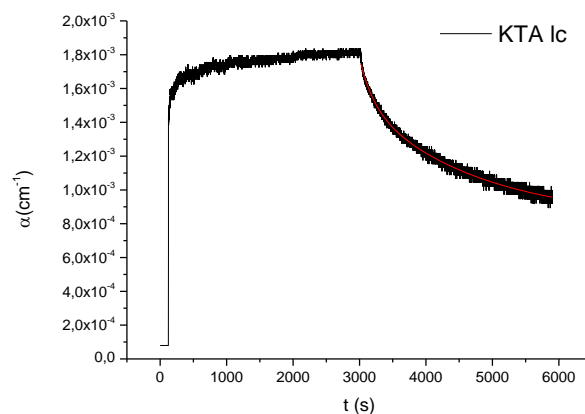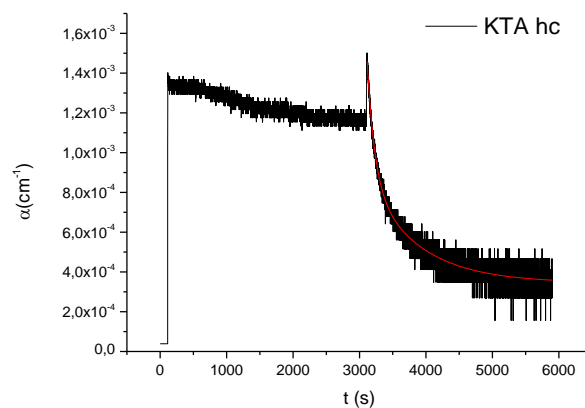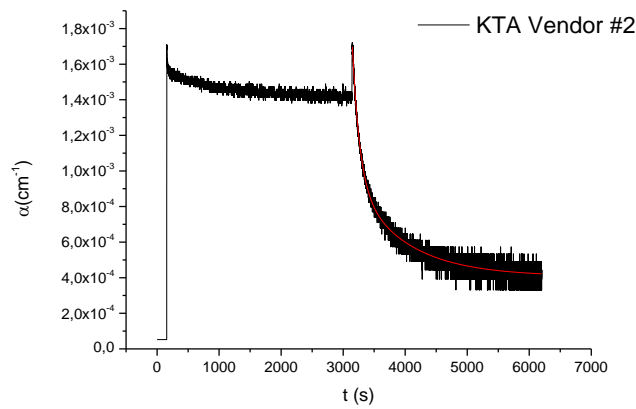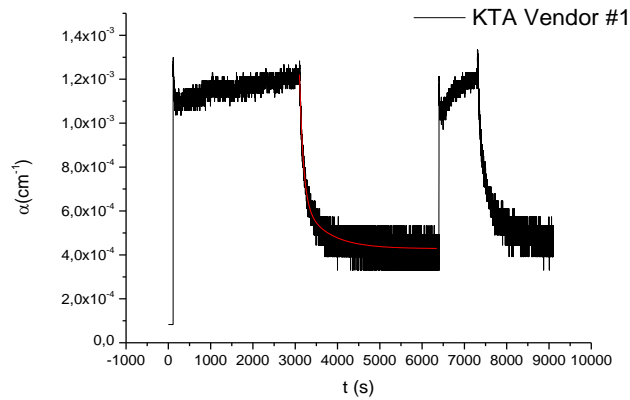
Figure 5.3 - BLIIRA in KTA samples from different vendors and with different conductivity

	α_{start} (cm^{-1})	A_1	τ_1 (s)	A_2	τ_2 (s)	α_0 (cm^{-1})
KTA hc	$3{,}89 \cdot 10^{-5}$	$5{,}27 \cdot 10^{-4}$	765	$6{,}84 \cdot 10^{-4}$	114	$3{,}45 \cdot 10^{-4}$
KTA lc	$7{,}98 \cdot 10^{-5}$	$6{,}73 \cdot 10^{-4}$	1752	$2{,}09 \cdot 10^{-4}$	212	$8{,}25 \cdot 10^{-4}$
KTA V#1	$8{,}28 \cdot 10^{-5}$	$2{,}22 \cdot 10^{-4}$	609	$7{,}39 \cdot 10^{-4}$	90	$4{,}29 \cdot 10^{-4}$
KTA V#8	$5{,}24 \cdot 10^{-5}$	$5{,}39 \cdot 10^{-4}$	836	$8{,}64 \cdot 10^{-4}$	118	$4{,}08 \cdot 10^{-4}$

Table 5.4

The crystal from Vendor #1 and the HC one show a good resistance to gray-tracks, with a maximum value for the absorption coefficient of $1{,}3 \cdot 10^{-3}$cm^{-1} in the first case, and $1{,}4 \cdot 10^{-3}$cm^{-1} for the second one. The induced absorption for the sample from Vendor #2 has values comparable with the case of RKTP. LC KTA on the other side, presents a high susceptibility to damage, reaching values of α around $1{,}8 \cdot 10^{-3}$cm^{-1}, i.e. about 40% higher than the most resistant sample. This high variability might be related to different growth techniques adopted by the vendors and the associated number of native defects. Table 5.4 shows a double-exponential decay with high values of both the time constants for the LC sample, while the three other crystals, characterized by an higher

conductivity, present much faster dynamics. We can then conclude that, as in the case of KTP, also here an higher conductivity is accompanied by a faster relaxation. The baseline level results much lower in the first three cases, with a good recovery from the damage, while LC KTA presents a strong residual grey-track.

5.1.4. RTP

In our samples of Rubidium Titanyl Phosphate, provided by two different vendors, the first thing that is noticed is the high sensitivity to BLIIRA, with α reaching values near to $6 \cdot 10^{-3} cm^{-1}$ during grey-tracking. Despite this difference then, the curves features are similar to the one we described for KTA. In RTP from Vendor #1 an initial overshoot is followed by a positive drift as the one observable in the first KTA sample. As well as in the Arsenate, the study of the memory effect doesn't show any particular change of the induced absorption during the second consecutive illumination with blue light.
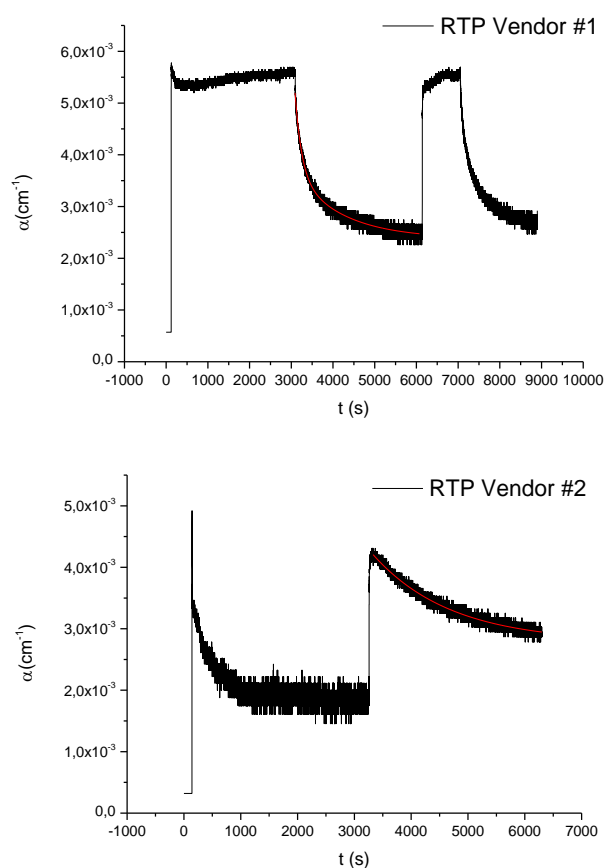
Figure 5.4 - BLIIRA in RTP samples from different vendors

	α_{start} (cm^{-1})	A_1	τ_1 (s)	A_2	τ_2 (s)	α_0 (cm^{-1})
RTP V#1	$5{,}71{\cdot}10^{-4}$	$1{,}28{\cdot}10^{-3}$	1151	$1{,}92{\cdot}10^{-3}$	160	$2{,}38{\cdot}10^{-3}$
RTP V#2	$3{,}21{\cdot}10^{-4}$	$7{,}28{\cdot}10^{-4}$	1368	-	-	$2{,}78{\cdot}10^{-3}$

<div align="right">Table 5.5</div>

The crystal from Vendor #2 shows instead an initial overshoot of BLIIRA and a negative drift, which reaches a stable value after approximately 20 minutes. Once the damaging beam is blocked, α jumps to higher values, showing then a single-exponential decay characterized by a long time constant. The residual damage for this crystal is much higher than in the RTP sample from Vendor #1, as the comparison between the two baselines in table 5.5 shows.

5.1.5. RTA

Rubidium Titanyl Arsenate shows a high sensitivity to BLIIRA when compared to KTP, RKTP or KTA, with an absorption coefficient reaching values around $3{\cdot}10^{-3}$cm^{-1}. Also here we identify a negative drift as in some KTA and RTP samples, but with a lower steepness and followed by a much lower jump. The crystal is the one presenting the slowest double-exponential relaxation dynamics.
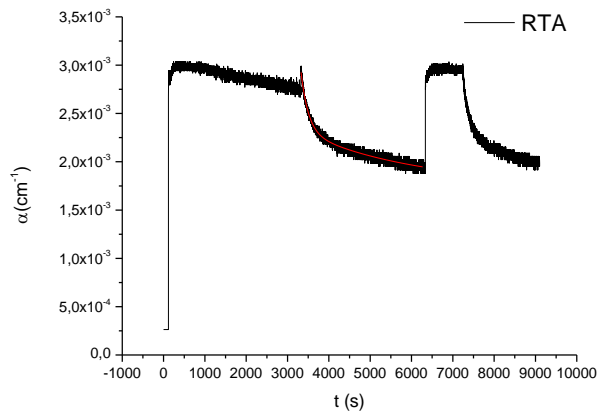
<div align="center">Figure 5.5 - BLIIRA in RTA</div>

	α_{start} (cm^{-1})	A_1	τ_1 (s)	A_2	τ_2 (s)	α_0 (cm^{-1})
RTA	$2{,}63{\cdot}10^{-4}$	$5{,}62{\cdot}10^{-4}$	2709	$6{,}45{\cdot}10^{-4}$	178	$1{,}76{\cdot}10^{-3}$

<div align="right">Table 5.6</div>

5.2. Damage Accumulation in KTP

The measurements on KTP and RKTP show through the repetitive exposure to the blue pulses, that a longer illumination with the damage-inducing beam results in a higher value of the baseline α_0. This is visible from the curves of HC KTP and HC RKTP #2. This feature, together with the fact that a second exposure to the damaging beam brings back α to the value that it used to have before relaxation, suggests that the damage slowly generated by the beam is the one characterized by long time constants (of the order of days). We studied this progressive accumulation of the damage repeating several times the process of exposure of the HC KTP crystal to blue pulses (15-20 minutes) and observation of the subsequent relaxation (20 minutes). The curve obtained is shown in figure 5.6, while in table 5.7 are the time constants for the different decays with their baselines.
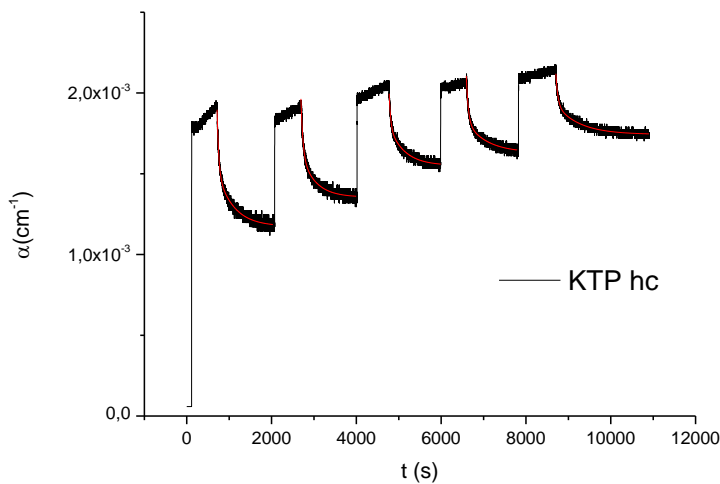
Figure 5.6 - BLIIRA measurement with repeated exposure to the damage-inducing beam

	A_1	τ_1 (s)	A_2	τ_2 (s)	α_0 (cm^{-1})
decay #1	$3{,}40 \cdot 10^{-4}$	385	$4{,}33 \cdot 10^{-4}$	38	$1{,}17 \cdot 10^{-3}$
decay #2	$2{,}65 \cdot 10^{-4}$	336	$3{,}62 \cdot 10^{-4}$	47	$1{,}36 \cdot 10^{-3}$
decay #3	$2{,}44 \cdot 10^{-4}$	364	$2{,}62 \cdot 10^{-4}$	35	$1{,}55 \cdot 10^{-3}$
decay #4	$1{,}92 \cdot 10^{-4}$	486	$3{,}19 \cdot 10^{-4}$	47	$1{,}63 \cdot 10^{-3}$
decay #5	$1{,}92 \cdot 10^{-4}$	560	$3{,}32 \cdot 10^{-4}$	48	$1{,}74 \cdot 10^{-3}$

Table 5.7

Apart from a monotonic rise of α_0, we notice also that the longer time constant τ_1 increases progressively, while its coefficient A_1 decreases. There is no such regular behaviour observable for the faster time constant. Plotting α_0 against

60

the cumulated exposure time (figure 5.7) it is possible to see that the relation between the two is not linear, but tends to saturate for longer exposure.
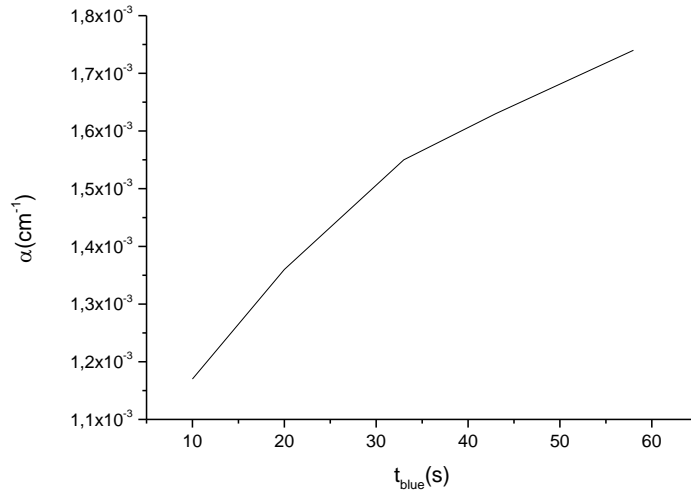
Figure 5.7 - Baseline growth in relation with the cumulated exposure time

The study of the damage relaxation reveals that grey-tracking is a complex mechanism involving different kind of traps and probably caused by various damaging processes. The multiple-exponential decay indicates that both shallow and deep traps are filled during the exposure to blue pulses, and the increasing baseline suggests a progressive rise of the population in deeper levels within the bandgap through a slow process, less probable than the ones that fill shallower traps.

5.3. Variation of BLIIRA with Temperature

Following a different procedure, which consisted in an exposure of 10 minutes to the grey-tracking beam and the following observation of the relaxation process for 20 minutes, we measured BLIIRA for different crystal temperatures. We choose a representative sample for each isomorphs group, recording the induced absorption dynamics at 25°C, 40°C, 60°C and 80°C. The four measurements are all carried out on the same crystal within the periodically poled area, but on different spots. Given the change of the boundary conditions we had to measure the signal from our BK7 reference sample for each temperature before starting.
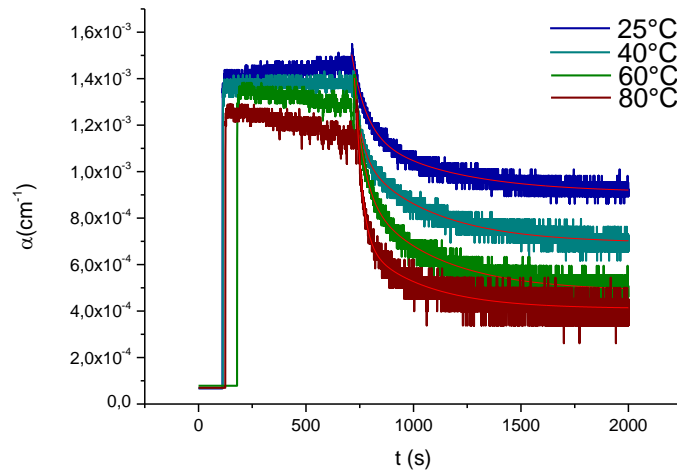
Figure 5.8 - BLIIRA at different temperatures in KTP

T(^{o}C)	A_1	τ_1(s)	A_2	τ_2(s)	α_0
25	$3,54 \cdot 10^{-4}$	66	$2,74 \cdot 10^{-4}$	406	$9,09 \cdot 10^{-4}$
40	$3,57 \cdot 10^{-4}$	37	$3,81 \cdot 10^{-4}$	346	$6,93 \cdot 10^{-4}$
60	$5,15 \cdot 10^{-4}$	45	$4,31 \cdot 10^{-4}$	348	$4,10 \cdot 10^{-4}$
80	$2,98 \cdot 10^{-4}$	30	$2,98 \cdot 10^{-4}$	293	$4,10 \cdot 10^{-4}$

Table 5.8
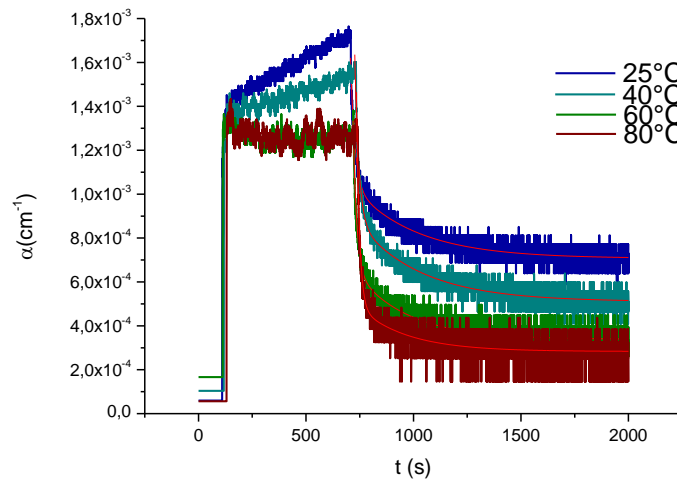
Figure 5.9 - BLIIRA at different temperatures in RKTP

T(^{o}C)	A_1	τ_1(s)	A_2	τ_2(s)	α_0
25	$1,23 \cdot 10^{-3}$	20	$3,55 \cdot 10^{-4}$	295	$7,07 \cdot 10^{-4}$
40	$1,33 \cdot 10^{-3}$	19	$3,90 \cdot 10^{-4}$	296	$6,93 \cdot 10^{-4}$
60	$1,27 \cdot 10^{-3}$	17	$3,32 \cdot 10^{-4}$	244	$3,38 \cdot 10^{-4}$
80	$1,44 \cdot 10^{-3}$	14	$2,14 \cdot 10^{-4}$	227	$2,83 \cdot 10^{-4}$

Table 5.9

Analyzing the curves of KTP and RKTP we notice that the change of BLIIRA dynamics is similar for both crystals. During exposure the drift to higher absorption levels becomes less and less steep with increasing T, reaching a negative slope for 60°C and 80°C; also the maximum induced absorption decreases, indicating a lower susceptibility at higher temperatures. Observing the time constants in tables 5.8 and 5.9 we notice that, as expected, the higher thermal energy means a shorter lifetime of the trap states, with faster relaxation of BLIIRA and also a lower baseline level. Some fluctuation from a monotonic decrease of the time constants are observable, but the reason for this might be attributed to the gathering of the measurement from multiple spots, presenting slightly different native defects.
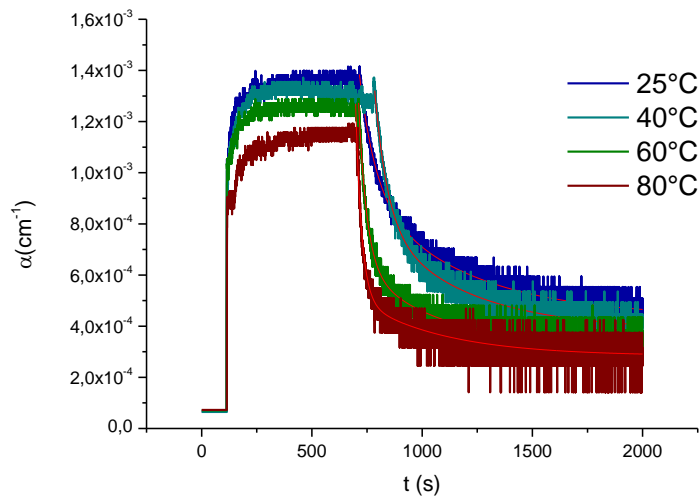
Figure 5.10 - BLIIRA at different temperatures in KTA

T(°C)	A_1	$\tau_1(s)$	A_2	$\tau_2(s)$	α_0
25	$4{,}80{\cdot}10^{-4}$	73	$4{,}96{\cdot}10^{-4}$	458	$4{,}36{\cdot}10^{-4}$
40	$5{,}73{\cdot}10^{-4}$	58	$4{,}23{\cdot}10^{-4}$	402	$3{,}85{\cdot}10^{-4}$
60	$7{,}89{\cdot}10^{-4}$	37	$3{,}21{\cdot}10^{-4}$	326	$3{,}29{\cdot}10^{-4}$
80	$9{,}13{\cdot}10^{-4}$	27	$2{,}27{\cdot}10^{-4}$	385	$2{,}84{\cdot}10^{-4}$

Table 5.10

The behaviour of KTA (figure 5.10) is similar to the one observed for KTP and RKTP, with decreasing time constants and baseline at higher temperatures but without any change in the curve shape during exposure, which remains flat in all the four cases.

RTP shows unexpected features, consisting in what looks like a permanent damage after exposure at higher temperature (80°C line in figure 5.11) and

extremely slow relaxation in the other cases. It is not possible to fit the decays with any exponential curve, and the damages remain visible for several days. The exposure causes a positive drift of α at 25°C, which becomes negative for higher temperatures. In all cases when the blue light is turned off the absorption undergoes a fast drop (compared to the relaxation times) followed by a rise and then again a final relaxation. This unusual behaviour could be related to a modification of internal lattice strain induced during annealing, which creates local fields with effects on BLIIRA. The annealing step is in fact the only process that could have changed the features of the induced absorption described in section 5.1.4. for RTP.
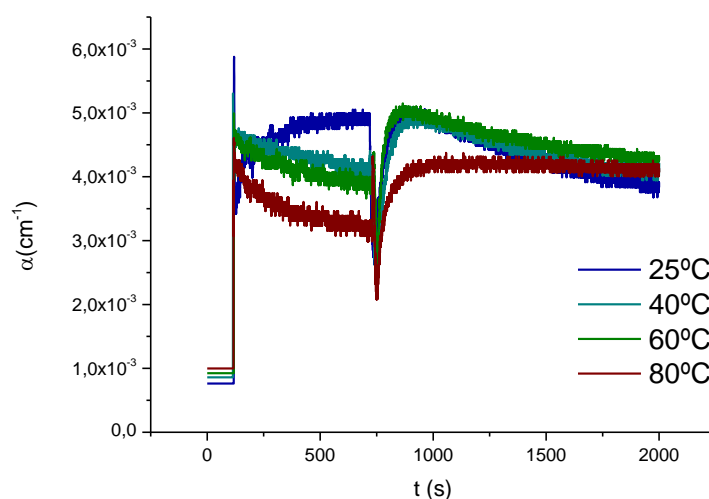
Figure 5.11 - BLIIRA at different temperatures in RTP

The aspect of BLIIRA changed also for RTA, presenting two overshoots at the beginning and at the end of the exposure, with a drift to lower values in between (figure 5.12). Here surprisingly the maximum absorption level increases with temperature, while the only relaxation quantity of table 5.11 that shows any correlation with temperature is the fast time constant, which decreases with increasing T.
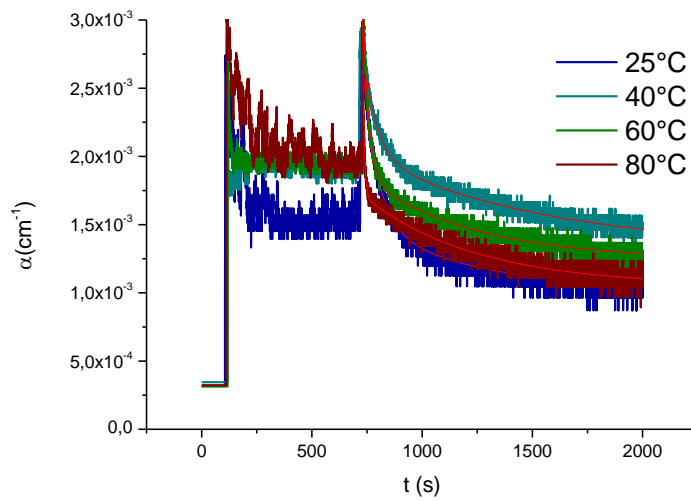
Figure 5.12 - BLIIRA at different temperatures in RTA

T(^{o}C)	A$_1$	τ_1(s)	A$_2$	τ_2(s)	α_0
25	$1,29 \cdot 10^{-3}$	65	$5,21 \cdot 10^{-4}$	463	$1,02 \cdot 10^{-3}$
40	$9,72 \cdot 10^{-4}$	58	$7,04 \cdot 10^{-4}$	799	$1,33 \cdot 10^{-3}$
60	$1,93 \cdot 10^{-3}$	26	$6,23 \cdot 10^{-4}$	500	$1,24 \cdot 10^{-3}$
80	$5,64 \cdot 10^{-3}$	7	$6,80 \cdot 10^{-4}$	508	$1,05 \cdot 10^{-3}$

Table 5.11

If the effect of local internal fields is strongly conditioning BLIIRA in both RTP and RTA the comparison between measurements performed on different parts of the crystals can't be always considered valid. It is important to remind of this consideration also in the studies carried out in the next section.

5.4. Variation of BLIIRA with Blue Pulses Duration

The regenerative amplifier stretches, amplifies and then compresses again the infrared pulses coming from a mode-locked Ti:Sapphire laser. The translation of one of the gratings belonging to the compressor stage allows us to tune the pulse length. We exposed the same five crystals used in the previous measurement to 2, 10, 20 and 40ps pulses, following the procedure where 10 minutes of illumination are followed by 20 minutes of relaxation. As in the other cases absorption of BK7 is measured daily as a reference.
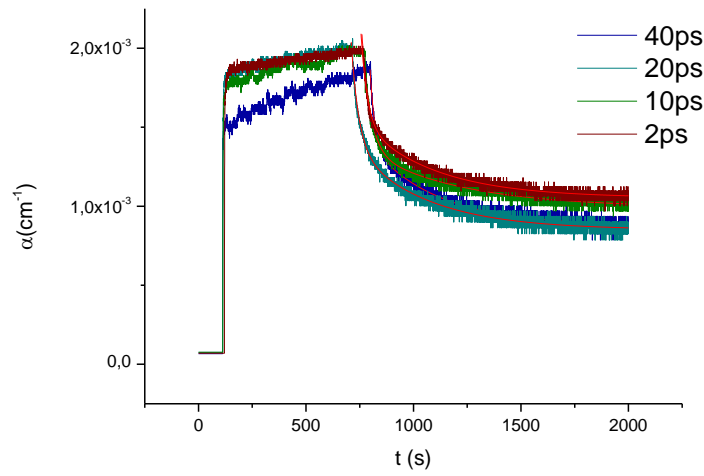
Figure 5.13 - BLIIRA with different blue pulses duration in KTP

τ(ps)	A_1	τ_1(s)	A_2	τ_2(s)	α_0
40	$6,33 \cdot 10^{-4}$	22	$5,12 \cdot 10^{-4}$	315	$8,77 \cdot 10^{-4}$
20	$8,18 \cdot 10^{-4}$	35	$5,41 \cdot 10^{-4}$	340	$8,51 \cdot 10^{-4}$
10	$7,96 \cdot 10^{-4}$	38	$3,72 \cdot 10^{-4}$	445	$9,91 \cdot 10^{-4}$
2	$5,20 \cdot 10^{-4}$	29	$4,69 \cdot 10^{-4}$	340	$1,05 \cdot 10^{-3}$

Table 5.12

Figure 5.14 - BLIIRA with different blue pulses duration in RKTP

τ(ps)	A_1	τ_1(s)	A_2	τ_2(s)	α_0
40	$9,91 \cdot 10^{-4}$	25	$3,84 \cdot 10^{-4}$	314	$7,08 \cdot 10^{-4}$
20	$8,04 \cdot 10^{-4}$	26	$3,81 \cdot 10^{-4}$	320	$7,56 \cdot 10^{-4}$
10	$6,71 \cdot 10^{-4}$	35	$3,16 \cdot 10^{-4}$	368	$8,62 \cdot 10^{-4}$
2	$4,64 \cdot 10^{-4}$	34	$3,41 \cdot 10^{-4}$	328	$8,13 \cdot 10^{-4}$

Table 5.13

Again KTP and RKTP show very similar features, as it is possible to see from figures 5.13 - 5.14 and tables 5.12 - 5.13. During the damage formation with longer pulses KTP shows slightly lower absorption values, while in RKTP the positive drift disappears for 2ps pulses. The two time constants and the baseline increase in both cases going from 40 to 10ps, but in KTP this trend is interrupted by a drop of τ_1 and τ_2 at 2ps. In RKTP not just the two time constants, but also the baseline value for the shortest pulse is lower than in the 10ps one.

In KTA we notice a change in BLIIRA during exposure, with a gradual decrease of the induced absorption for shorter pulses. What happens is that when the damaging beam is switched on α reaches a value around $1,9\cdot10^{-3}cm^{-1}$, then it suddenly jumps down as there was some mechanism of inhibition of the induced absorption growing stronger for higher intensities. For shorter pulses the jump arrives down to lower absorption levels, and then a drift starts, with approximately the same negative slope in all cases. Once the process ends and the blue light is turned off, α jumps back to higher values around $2\cdot10^{-3}cm^{-1}$ and from there starts a relaxation that is clearly pulse length-independent, as the dynamics depicted in figure 5.15 demonstrate.
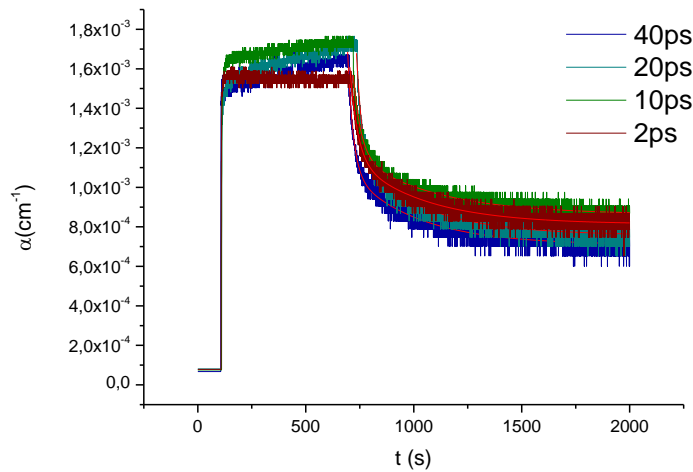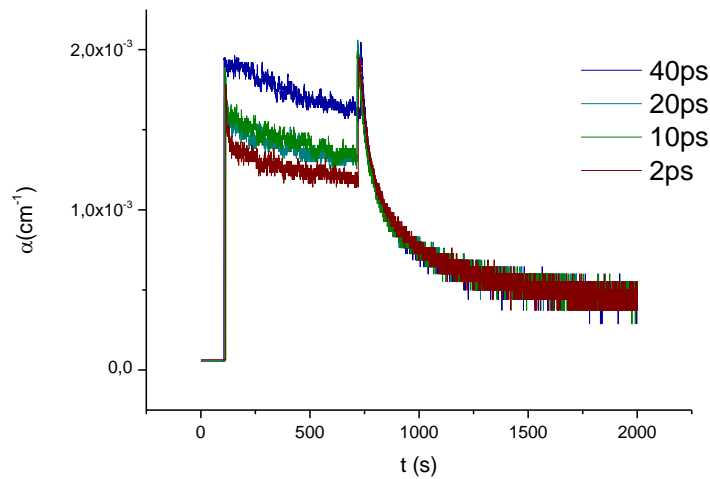

Figure 5.15 - BLIIRA with different blue pulses duration in KTA

τ(ps)	A_1	τ_1(s)	A_2	τ_2(s)	α_0
40	$1,09\cdot10^{-3}$	40	$6,69\cdot10^{-4}$	346	$4,40\cdot10^{-4}$
20	$1,10\cdot10^{-3}$	50	$6,49\cdot10^{-4}$	408	$4,37\cdot10^{-4}$
10	$1,05\cdot10^{-3}$	45	$6,67\cdot10^{-4}$	378	$4,38\cdot10^{-4}$
2	$7,61\cdot10^{-4}$	48	$6,83\cdot10^{-4}$	365	$4,34\cdot10^{-4}$

Table 5.14

67

The studies on RTP were inconclusive as in the previous section, showing unexpected curves without any direct correlation between pulse duration and induced absorption (low for 2 and 40ps pulses and higher in the two other cases). Even if it is not possible to fit the decay of BLIIRA, the relaxation looks like having the same baseline for all cases. After exposure a slow return to higher values of α is more pronounced for longer pulses, and disappears for 2ps pulses.
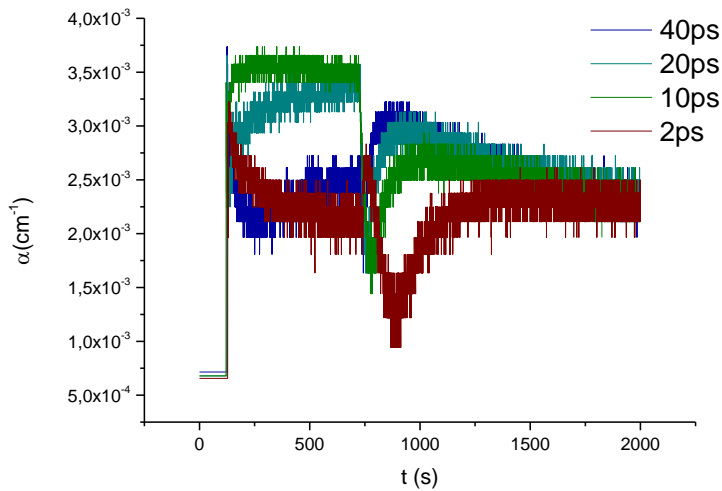
Figure 5.16 - BLIIRA with different blue pulses duration in RTP

The induced absorption inhibition is present in RTA as it was in KTA, but unlike the other arsenate, relaxation leads to a high baseline indicating a strong residual damage with long decay constant, and a colouration that lasts for several days. As well as in RTP the curve can't be fitted with any exponential expression.
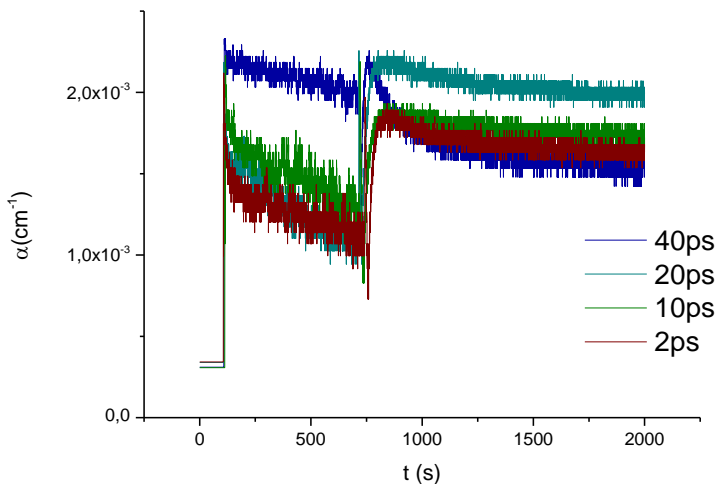
Figure 5.17 - BLIIRA with different blue pulses duration in RTA

Comparing BLIIRA curves for KTA and RTA we notice that the behaviour has changed from the one described in previous sections, so we must deduce that the annealing step influenced again the response of the crystals to the damaging beam.

5.5. Variation of BLIIRA with Blue Average Power

For our last measurements we decided to record BLIIRA just in KTP and KTA, given the inconclusive results previously obtained on RTP and RTA and the similarities between KTP and RKTP which probably derive from the almost unchanged crystal structure of the two compounds. The average power of the blue pulses is changed to 1, 3, 6 and 9mW fixing the pulse length at 30ps. BLIIRA is recorded at ambient temperature (25°C) with the same exposure and relaxation times used before.
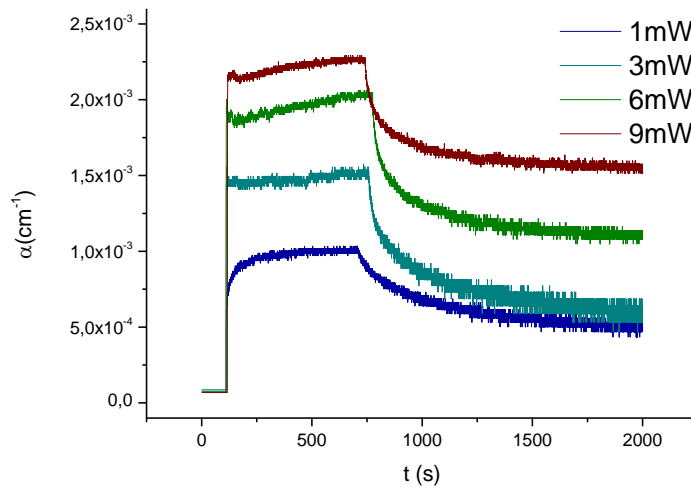
Figure 5.18 - BLIIRA at different blue pulses average power in KTP

P(mW)	A_1	τ_1(s)	A_2	τ_2(s)	α_0
1	$1,75 \cdot 10^{-4}$	72	$3,76 \cdot 10^{-4}$	511	$4,72 \cdot 10^{-4}$
3	$4,90 \cdot 10^{-4}$	29	$5,37 \cdot 10^{-4}$	392	$5,87 \cdot 10^{-4}$
6	$6,48 \cdot 10^{-4}$	24	$4,67 \cdot 10^{-4}$	293	$1,10 \cdot 10^{-3}$
9	$5,32 \cdot 10^{-4}$	30	$3,45 \cdot 10^{-4}$	296	$1,55 \cdot 10^{-3}$

Table 5.15

The increased intensity produces an higher induced absorption in KTP as previously reported by several authors [19,42], with a nonlinear correlation between intensity and maximum absorption level. Also the residual baseline

follows the same trend. In KTA the induced absorption grows at first, passing from 1mW to 3mW, but then drops to the lowest value for 6mW pulses and comes back to the level it had at the beginning for 9mW. The low intensity beams don't generate any negative drift or jump, while these features show up for 6mW and 9mW pulses.
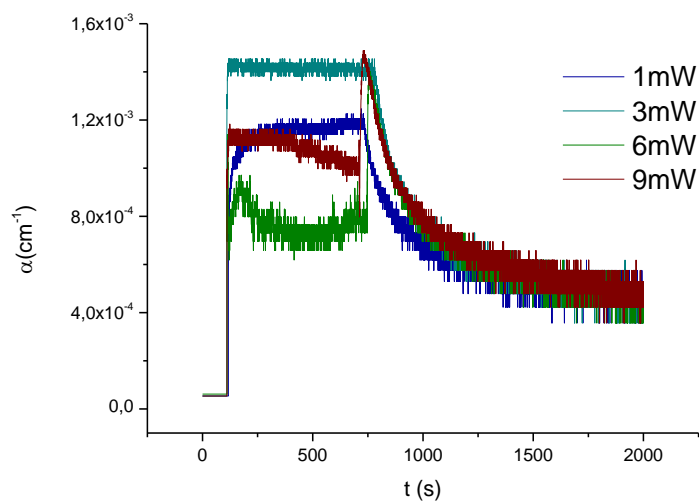
Figure 5.19 - BLIIRA with different blue pulses average power in KTA

P(mW)	A_1	$\tau_1(s)$	A_2	$\tau_2(s)$	α_0
1	$3{,}03 \cdot 10^{-4}$	61	$4{,}47 \cdot 10^{-4}$	413	$4{,}52 \cdot 10^{-4}$
3	$5{,}13 \cdot 10^{-4}$	75	$5{,}03 \cdot 10^{-4}$	476	$4{,}33 \cdot 10^{-4}$
6	$5{,}20 \cdot 10^{-4}$	90	$5{,}00 \cdot 10^{-4}$	525	$4{,}15 \cdot 10^{-4}$
9	$5{,}23 \cdot 10^{-4}$	93	$5{,}24 \cdot 10^{-4}$	539	$4{,}32 \cdot 10^{-4}$

Table 5.16

70

Discussion and Conclusions

The study of the BLIIRA effect in periodically poled crystals from the KTP family has been reported, and the comparison of the gathered data with previous papers confirm some of the behaviour already observed in KTP and RKTP, bringing also some novelty elements. The studies carried out on KTA, RTP and RTA, together with the analysis of isomorphs with different conductivities have brought new elements useful for the understanding of this damaging process.

Despite the similar features of the acquired BLIIRA curves of RKTP and KTP, Rubidium doped KTP shows a higher resistance to the damage, a fact that is in agreement with the studies on grey-tracking made by Žukauskas et al. [24]. The measured intrinsic absorption coefficient for both crystals is around $5 \cdot 10^{-5} cm^{-1}$; blue picosecond pulses cause in KTP a rise of this value up to $1{,}5\text{-}2 \cdot 10^{-3} cm^{-1}$, depending on the exposure time. These measurements are in accordance with the ones reported by Wang [18] and Hirohashi [19]. The absorption coefficient in RKTP remains always lower than $2 \cdot 10^{-3} cm^{-1}$, even after prolonged exposure. KTA shows in general a lower sensitivity to grey tracks when compared to KTP, but this characteristic is not uniform among crystals from different vendors. Finally RTP and RTA show the lowest resistance to BLIIRA, with values in a wide range between 2 and $6 \cdot 10^{-3} cm^{-1}$.

We can identify a correlation between conductivity and relaxation times in KTP and KTA, with longer time constants characterizing BLIIRA decay in samples with lower conductivity. Even if this correlation is not present in RKTP, in general we can observe that isomorphs containing Rubidium (especially RTP and RTA) show longer relaxation times than those containing only Potassium. This feature is not immediately visible from the BLIIRA plots of the various crystals because of the different residual baseline, which is not depending on Rubidium presence. The different mobility of the cations, then, results in an important factor influencing the damaging features of these nonlinear crystals.

In KTP and RKTP the damage formation has a fast initial rise and a slower drift leading to higher absorption levels, with dynamics similar to the one described by Mürk et al. [14] for grey-tracking formation. This confirms then a model where the initial stage of colouration is related with recharging of traps from native defects, while the following slow increase in absorption is due to radiation-induced defects. Another behaviour previously reported for periodically poled KTP [18] has been observed here in some KTA, RTP and RTA

isomorphs. The exposure to the damaging beam produces an initial overshoot of the absorption which decreases rapidly in the first few seconds, and then continues to slowly drift over time towards lower values. After blocking the beam, α jumps back to what was approximately its initial value, and then starts to relax with a double-exponential decay. The reports on KTP attributed this behaviour to residual strain present inside the materials, which were not annealed after the poling process. Our samples were all annealed before usage, and we can suppose that the complete substitution of Rubidium for Potassium and of Arsenic for Phosphorus creates compound with stronger local strain, which can be modified, but not removed with annealing at 250°C.

In KTP, as we said, the progressive increase in absorption during exposure is attributed to beam-induced defects. Studying this process with repeated blue pulses illumination it has been shown that the baseline of the relaxation raises with the exposure time, meaning that the generated damage, which is modelled as permanent in our fit, presents much slower decay dynamics than the others. The time constant can be estimated of the order of days, since a further relaxation below the baseline is observable, even without annealing, the day after the experiment.

The rise of temperature induces faster relaxation in KTP, RKTP, KTA and RTA, with a better recovery from the damage at higher temperatures. During exposure the rise of T is also accompanied by a decrease of the maximum induced absorption in KTP, RKTP and KTA, together with a lowering of the drift slope in KTP and RKTP, which passes from positive to negative for temperatures over 40°C. In RTA we observe a different behaviour, with an increased sensitivity at higher temperatures during illumination with blue pulses.

In KTP and RKTP the different pulse duration has mild effects on BLIIRA, while it influences most KTA and RTA, where the shorter pulses cause a stronger inhibition of the induced absorption during exposure. The higher intensity obtained through an increase of the blue pulses average power produces a stronger BLIIRA in KTP, in agreement with previous reports [19,42], while in KTA results in a non monotonic trend of the induced absorption.

After the first measurement, RTP shows a completely different behaviour, with incomparable damaging dynamics observed in different spots of the same crystal. We consider the measurements carried out after the first annealing step as inconclusive.

The study on many KTP isomorphs and in various experimental conditions described in this paper can be considered as a new step for a better understanding of the BLIIRA mechanisms. The importance of conductivity, of the presence of larger or smaller cations, the different damaging dynamics and even the possible role of internal strain causing unexpected results, are all phenomena leading to new hypothesis and paths for future researches. A complete knowledge of BLIIRA could bring to novel solutions for the growth of grey-tracking-resistant (or at least BLIIRA-resistant) materials, opening to new records of conversion efficiency from the near infrared to the blue-green wavelengths. Not only SHG, but any other application involving illumination of KTP isomorphs with blue light would benefit from this improvement, given the elimination of induced absorption in a wide range of frequencies.

Possible Future Studies

For a deeper understanding of BLIIRA it will be important to focus on a more precise study of the correlation between crystals internal strain and induced absorption dynamics. Especially in RTP a further analysis of the strain effects after annealing is needed.

Since the measurements for different pulse lengths didn't show any significant result in KTP and RKTP, the characterization of BLIIRA over a wider range of pulse durations, including also nanoseconds pulses, could be interesting for future in-depth analysis.

Following the same reasoning for the temperature range, which in our case was limited by the low thermal resistance of the Peltier cell and of the thermal glue, the possibility of a study at higher temperatures could determine exactly when BLIIRA effects disappear, and help to identify the relaxation processes involved.

In this experiment we could not analyze the formation of BLIIRA, since the fast initial rise was masked by the lock-in amplifier integration. With the observation of this process it would be possible to have a better understanding of the dynamics of the trapping mechanisms causing grey-tracking.

Bibliography

[1] H. Karlsson *"Fabrication of periodically poled crystals from the KTP family and their applications in nonlinear optics"* Department of Laser Physics and Quantum Optics, The Royal Institute of Technology, Stockholm, Sweden

[2] M. N. Satyanarayan, A. Deepty, H. L. Bhat *"Potassium Titanyl Phosphate and Its Isomorphs: Growth, Properties and Applications"* Critical Reviews in Solid State and Material Sciences, 24:2, pp. 103-191 (1999)

[3] C. Canalias, J. Hirohashi, V. Pasiskevicius, F. Laurell *"Polarization-switching characteristics of flux-grown $KTiOPO_4$ and $RbTiOPO_4$ at room temperature"* Journal of Applied Physics, Vol. 97, 124105 (2005)

[4] J. D. Bierlein, H. Vanherzeele *"Potassium titanyl phosphate: properties and new applications"* Journal of the Optical Society of America, Vol. 6, No.4 (1989)

[5] A. Žukauskas *"QPM devices in KTA and RKTP"* Doctoral Thesis, Department of Applied Physics KTH, Royal Institute of Technology

[6] V. Pasiskevicius, G. Stromqvist, F. Laurell, C. Canalias *"Quasi-phase matched nonlinear media: Progress towards nonlinear optical engineering"* Optical Materials, Vol. 34, pp. 513-523 (2012)

[7] N. I. Sorokina, V. I. Voronkova *"Structure and Properties of Crystals in the Potassium Titanyl Phosphate Family: A Review"* Crystallography Reports, Vol. 52, No. 1, pp 80-93 (2007)

[8] G. D. Stucky, M. L. F. Phillips, T. E. Gier *"The Potassium Titanyl Phosphate Structure Field: A Model for New Nonlinear Optical Materials"* Chemistry of Materials, Vol. 1, No. 5 (1989)

[9] G. M. Loiacono, D. N. Loiacono, T. McGee, M. Babb *"Laser damage formation in $KTiOPO_4$ and $KTiOAsO_4$ crystals: Grey tracks"* Journal of Applied Physics, Vol. 72, 2705 (1992)

[10] B. Boulanger, M. M. Fejer, R. Blachman, P. F. Bordui *"Study of $KTiOPO_4$ greytracking at 1064, 532, and 355nm"* Applied Physics Letters, Vol. 65, 2401 (1994)

[11] M. P. Scripsick, D. N. Loiacono, J. Rottenberg, S. H. Goellner, L.E. Halliburton, F. K. Hopkins *"Defects responsible for grey tracks in fluxgrown KTiOPO$_4$"* Applied Physics Letters, Vol. 66, 3428 (1995)

[12] L. E. Halliburton, M. P. Scripsick *"Mechanisms and point defects responsible for the formation of gray tracks in KTP"* Proc. of SPIE 2379, Solid State Lasers and Nonlinear Crystals, 235 (1995)

[13] V. A. Maslov, V. A. Mikhailov, O. P. Shaunin, I. A. Shcherbakov *"Nonlinear absorption in KTP crystals"* Quantum Electronics, Vol. 27, No.4, pp. 356-359 (1997)

[14] V. Mürk, V. Denks, A. Dudelzak, P. P. Proulx, V. Vassiltsenko *"Grey tracks in KTiOPO$_4$: Mechanisms of creation and bleaching"* National Instruments and Methods in Physics Research B 141, pp. 472-476 (1998)

[15] B. Boulanger, I. Rousseau, J. P. Fève, M. Maglione, B. Ménaert, G. Marnier *"Optical Studies of Laser-Induced Grey-Tracking in KTP"* Journal of Quantum Electronics, Vol. 35, No. 3 (1999)

[16] A. Deepthy, M. N. Satyanarayan, K. S. R. K. Rao, H. L. Bhat *"Photoluminescence studies on gray tracked KTiOPO$_4$ single crystals"* Journal of Applied Physics, Vol. 85, 8332 (1999)

[17] C. Zaldo, J. Carvajal, R. Solé, F. Diaz, D. Bravo, A. Kling *"Influence of impurities on the optical damage of KTiOPO$_4$ crystals"* Journal of Applied Physics, Vol. 88, 3242 (2000)

[18] S. Wang, V. Pasiskevicius, F. Laurell *"Dynamics of green light-induced infrared absorption in KTiOPO$_4$ and periodically poled KTiOPO$_4$"* Journal of Applied Physics, Vol. 96, No. 4 (2004)

[19] J. Hirohashi, V. Pasiskevicius, S. Wang, F. Laurell *"Picosecond blue-light-induced infrared absorption in single-domain and periodically poled ferroelectrics"* Journal of Applied Physics, Vol. 101, 033105 (2007)

[20] S. Nagano, R. Shimizu, A. Shoji, K. Suizu, K. Edamatsu *"Temperature dependence of blue light-induced near-infrared absorption of ferroelectric crystals"* Conference on Lasers and Electro-Optics and Conference on Quantum Electronics and Laser Science (2008)

[21] H. T. Huang, G. Qiu, B. T. Zhang, J. L. He, J. F. Yang, J. L. Xu *"Comparative study on the intracavity frequency-doubling 532nm laser based on grey-tracking-resistant KTP and conventional KTP"* Applied Optics, Vol. 48, No. 32 (2009)

[22] Q. Zhang, G. Feng, J. Han, B. Li, Q. Zhu, X. Xie *"High repetition rate laser pulse induced damage in KTP crystal: Grey-tracking and catastrophic damage"* Optik, Vol. 122, pp. 1313-1318 (2011)

[23] O. A. Louchev, H. Hatano, N. Saito, S. Wada, K. Kitamura *"Laser-induced breakdown and damage generation by nonlinear frequency conversion in ferroelectric crystals: Experiment and theory"* Journal of Applied Physics, Vol. 114, 203101 (2013)

[24] A. Žukauskas, V. Pasiskevicius, C. Canalias *"Second-harmonic generation in periodically poled bulk Rb-doped KTiOPO$_4$ below 400nm at high peak intensities"* Optics Express, Vol. 21, No. 2 (2013)

[25] R. W. Boyd *"Nonlinear Optics, Third Edition"* Academic Press (2008)

[26] A. M. Weiner *"Ultrafast Optics"* Wiley Series in Pure and Applied Optics (2009)

[27] S. Tjörnhammar *"Thermal properties of volume Bragg gratings and its implications on lasers"* Licentiate Thesis, Department of Applied Physics KTH, Royal Institute of Technology

[28] C. Canalias *"Domain engineering in KTiOPO$_4$"* Doctoral Thesis, Department of Applied Physics KTH, Royal Institute of Technology

[29] J. Hirohashi *"Characterization of domain switching and optical damage properties in ferroelectrics"* Doctoral Thesis, Department of Applied Physics KTH, Royal Institute of Technology

[30] D. C. Clark, M. K. Kim *"High-precision method for measuring the photothermal properties of transparent media with digital holography"* Chinese Optics Letters, Vol. 9, No. 12 (2011)

[31] A. Marcano, C. Loper, N. Melikechi *"High-sensitivity absorption measurement in water and glass samples using a mode-mismatched pump-probe thermal lens method"* Applied Physics Letters, Vol. 78, 3415 (2001)

[32] M. Roth, N. Angert, M. Tseitlin, A. Alexandrowski *"On the optical quality of KTP crystals for nonlinear optical and electro-optic applications"* Optical Materials, Vol. 16, pp. 131-136 (2001)

[33] A. Alexandrowski, M. Fejer, A. Markosyan, R. Route *"Photothermal common-path interferometry (PCI): new developments"* Proc. of SPIE 7193, Solid State Lasers XVIII: Technologies and Devices (2009)

[34] S. E. Bialkowski *"Photothermal spectroscopy methods for chemical analysis"* John Wiley & Sons (1996)

[35] A. Marcano *"Pump-probe mode-mismatched thermal-lens Z scan"* Journal of the Optical Society of America B, Vol. 19, No. 1 (2002)

[36] A. Alexandrowski, G. Foulon, L. E. Myers, R. K. Route, M. M. Fejer *"UV and visible absorption in LiTaO$_3$"* Part. of SPIE, Laser Material Crystal Growth and Nonlinear Materials and Devices (1999)

[37] C.A. Ebbers, S. P. Velsko *"Optical and thermo-optical characterization of KTP and its isomorphs for 1.06μm pumped OPO's"* Photonic West: Conference on quantum well and superlattice physics (1996)

[38] J. D. Bierlein, H. Vanherzeele *"Potassium Titanyl phosphate: properties and new applications"* Journal of the Optical Society of America, Vol. 6, No. 4 (1989)

[39] D. N. Nikogosyan *"Nonlinear Optical Crystals: A Complete Survey"* Springer Science+Business Media (2005)

[40] J.J. Carvajal, P. Segonds, A. Pena, J. Zaccaro, B. Boulanger, F. Diaz, M. Aguilo *"Structural and optical properties of RbTiOPO$_4$:Nb crystals"* Journal of Physics: Condensed Matter, Vol. 19, 116214 (2007)

[41] F. C. Zumsteg, J. D. Bierlein, T.E. Gier *"K$_x$Rb$_{1-x}$TiOPO$_4$: A new nonlinear optical material"* Journal of Applied Physics, Vol. 47, 4980 (1976)

[42] J. Hirohashi, V. Pasiskevicius, F. Laurell, M. Kato, N. Saito, S. Wada *"Photochromic damage in nonlinear crystals for high-peak power blue light generation"* European Conference on Lasers and Electro-Optics and the International Quantum Electronics Conference (2007)

[43] L.E. Busse, L. Goldberg, M. R. Surette, G. Mizell *"Absorption losses in MgO doped and undoped potassium niobate"* Journal of Applied Physics, Vol. 75, 1102 (1994)

[44] H. Mabuchi, E. S. Polzik, H. J. Kimble *"Blue-light-induced infrared absorption in KNbO$_3$"* Journal of the Optical Society of America, Vol. 11, No. 10 (1994)

[45] D. Xue, S. Zhang *"The origin of nonlinearity in KTiOPO$_4$"* Applied Physics Letters, Vol. 70, 943 (1997)

[46] G. Rosenman, A. Skliar, I. Lareah, N. Angert, M. Tseitlin, M. Roth *"Observation of ferroelectric domain structures by secondary-electron microscopy in as-grown KTiOPO$_4$ crystals"* Physical Review B, Vol. 54, No. 9 (1996)

[47] L. K. Cheng, L. T. Cheng, J. D. Bierlein, F. C. Zumsteg, A. A. Ballman *"Properties of doped and undoped crystals of single domain KTiOAsO$_4$"* Applied Physics Letters, Vol. 62, 346 (1993)

[48] R. Blachman, P. F. Bordui, M. M. Fejer *"Laser-induced photochromic damage in potassium titanyl phosphate"* Applied Physics Letters, Vol. 64, 1318 (1994)

[49] L. A. Skvortsov *"Laser photothermal spectroscopy of light-induced absorption"* Quantum Electronics, Vol. 43, No.1, pp. 1-13 (2013)

[50] A. A. Lagatsky, N. V. Kuleshov, V. P. Mikhailov *"Diode-pumped CW lasing of Yb:KYW and Yb:KGW"* Optics Communications 165, pp. 71-75 (1999)

[51] G. H. Kim, J. Yang, D. S. Lee, A. V. Kulik, E. G. Sall, S. A. Chizov, V. E. Yashin, U. Kang *"High-power efficient cw and pulsed lasers based on bulk Yb:KYW crystals with end diode pumping"* Quantum Electronics, Vol. 42, No.4, pp. 292-297 (2012)

[52] G. Rosenman, A. Skliar, D. Edger, M. Oron, M. Katz *"Low temperature periodic electrical poling of flux-grown KTiOPO$_4$ and isomorphic crystals"* Applied Physics Letters, Vol. 73, 3670 (1998)

[53] G. Hansson, H. Karlsson, S. Wang, F. Laurell *"Transmission measurements in KTP and isomorphic compounds"* Applied Optics, Vol. 39, No. 27 (2000)

[54] D. Geskus, E. H. Bernhardi, K. van Dalfsen, S. Aravazhi, M. Pollnau *"Highly efficient Yb^{3+}-doped channel waveguide laser at 981nm"* Optics Express, Vol. 21, No. 11 (2013)